SWISS FEDERAL INSTITUTE OF TECHNOLOGY ZURICH

ETH*zürich*

Ocean Heat Storage And Implications On Sea Level Rise Using CCSM4 Model Output For 1993 - 2016

by

Maurice Huguenin-Virchaux

at the

Institute of Atmospheric and Climate Science

Prof. Dr. Reto Knutti

Supervisor: Dr. Iselin Medhaug

June 30th, 2016

Abstract

by Maurice Huguenin-Virchaux

Ocean heat uptake and storage is a key component in regulating the global climate system and is leading to sea level rise by thermal expansion. This thesis presents an analysis based on the output from the general circulation model CCSM4 for the time period 1993 - 2016 and shows that ocean heat storage is highest in the Southern and North Atlantic Ocean. A total of 2.24×10^{23} Joule have been accumulated during the last 24 years, 70% is stored in the upper 700 m. A comparison with observed data sets shows that the model slightly overestimates (underestimates) global 700 m (2000 m) heat storage for 1993 - 2015 (2005 - 2015). Modelled upper 700 m heat accumulation is dominated by the Southern Ocean's latitude band $\pm30°$S. A considerable warming trend in the ocean waters, high surface absorption of heat around Antarctica in connection with a consistent northward transport of water masses transfers the warming signal into depths of 800 - 1000 m below warmer subtropical water. Due to low initial temperature conditions of $2 - 3°$C during heat uptake, thermosteric sea level in this region is minimal. On the contrary, modelled Atlantic Ocean heat storage influences sea level rise trends in its basin by up to 5 mm/year or twice the amount of the observed total mean annual sea level rise for this time-period. High heat uptake and subsequent deepwater formation in high latitudes transports 0.66×10^{23} Joule, or 40% of the global heat anomaly, into depths of $1500 - 2500$m although this basin only covers 17% of the ocean. The main components governing thermosteric sea level rise are identified as the initial temperature and salinity conditions during heat uptake, the magnitude of the ocean water's warming trends and the strength of the model's ocean circulation which transports the heat signal into the ocean's interior.

Acknowledgements

I would like to thank Prof. Dr. Reto Knutti who allowed me to write my thesis in his working group. I would also like to thank my supervisor Dr. Iselin Medhaug for giving me supportive assistance throughout this journey. Without her, this thesis would not have been possible. She set aside many hours to help me with the Matlab calculations and with the concepts on how to best visualize the data sets. She supported me on how to structure my thesis in order to clearly present the main message so that a story evolved. I would like to thank her for reading through initial drafts of my thesis, for providing useful feedback, links to interesting papers and for always answering emails quickly.

My gratitude also extends to my brothers and sister for reading through my thesis and giving me feedback as well as my parents for their continuous support.

Contents

Chapter 1: Introduction

Human influence on the climate system since the nineteenth century through emission of greenhouse gases has led to an imbalance in the Earth's energy budget resulting in increased temperatures in the oceans and melting glaciers and ice-sheets. In the recent decades, over 90% of the additional energy has been directly stored in the ocean and lead to its volume increase by warming and subsequent expanding (Johnson and Lyman, 2014, Gleckler et al., 2016). Thermal expansion is therefore of considerable importance and is one of the largest contributors to global mean sea level rise (Cazenave and Llovel, 2010).

Changes in sea level relative to the land surface have been measured since the nineteenth century by tide gauges (Douglas et al., 2000) (see the grey shaded area in Figure 1.1a. Estimates for the preceding time were used to guess relative sea surface height before the industrial revolution. Since the early 1990s satellite altimetry, the up to today most precise and consistent measurement type, has been used. Hereby, microwave radiation emitted from the instrument measures the height above a fixed reference surface (Cazenave and Llovel, 2010). Data obtained from satellites shows a global mean sea level rise of 2.9 [2.5 to 3.4] mm/year for the last 24 years (as shown in Figure 1.1b). Climate models project future sea level rise in dependence of future greenhouse gas emission scenarios and with an uncertainty range from the year 2005 onwards (Bindoff et al., 2007) (see the blue shaded area in Figure 1.1a.
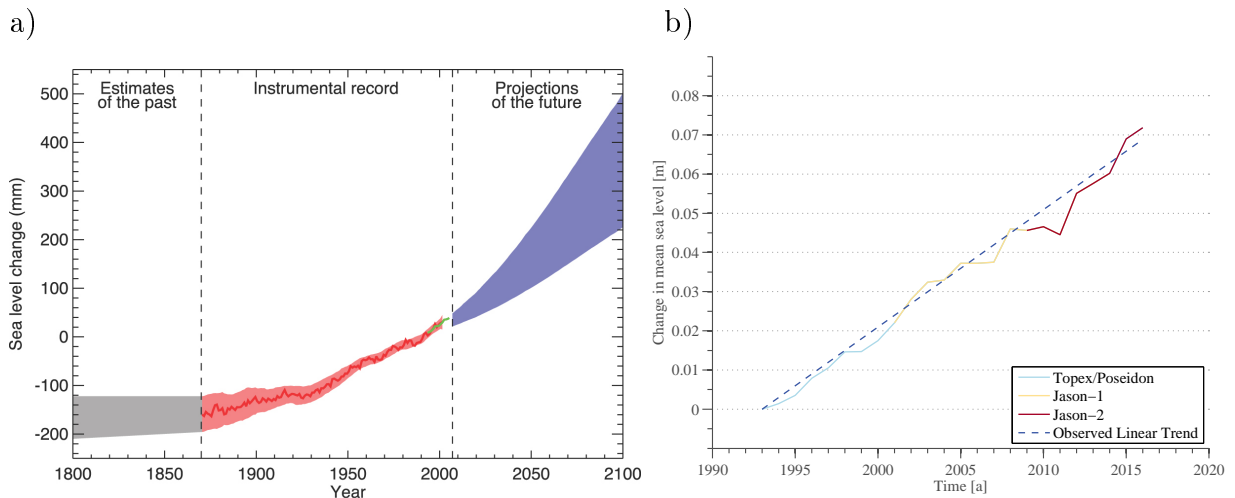
a)   b)

FIGURE 1.1: Evolution of estimated, observed and projected global mean sea level rise for a) $1800 - 2100$ and b) observed data for $1993 - 2016$. The grey shading in a) shows the uncertainty in the estimated long-term rate until 1870, the instrumental era including in red tide gauge and in green satellite and ocean float derived data until present days. The blue area represents future model projections with uncertainty ranges until the end of the century. Figure taken from (Bindoff et al., 2007). In b) satellite data shows the mean annual sea level rise from the three successive satellite programs Topex/Poseidon, Jason-1 and Jason-2 as well as in blue its associated linear trend of 2.9 mm/year. See also Section 3.1 on the source of this figure.

A variety of processes and components contribute to changes in sea level on different time and spatial scales (see Figure 1.2). The global ocean mass is affected by freshwater input of melting glaciers or ice-sheets and changes in the land hydrological cycle (Riva et al., 2010). The global ocean volume can change due to warming and subsequent expansion of its water masses or as a result of changes of the Earth's visco-elastic crust through subsidence and uplift (Church et al., 2013). Tectonic changes like glacial isostatic adjustment, i.e. slow uplift of the Earth's crust as a result of missing ice sheet mass, are slow and therefore insignificant for the here investigated time period. On regional scales, sea level rise is mostly influenced by density and circulation changes in the ocean and atmosphere and also impacted by thermal expansion. For example an increase in trade wind intensity in the Pacific may push warm water masses to its western border and leads to an increase in sea level in this region (England et al., 2014) (trade winds are easterly surface winds found near the equator). At the same time, cold water masses in the eastern Pacific get upwelled to balance out the missing mass. Wind and ocean circulation lead to a pile-up of water and additionally to a redistribution of heat. Since warm water of the same

mass has a higher volume than cold water, sea level is therefore increasing in the west while simultaneously decreasing in the east. Those cold water masses have higher density and do not impact sea level as much as the warm masses at the other side of the basin (England et al., 2014). Sea level extremes, caused by weather events like Hurricanes and Tsunamis, are occurring rapidly, affect local sea level on a short time-span and are also of insignificant importance to this thesis.

This thesis will focus on the blue coloured thermal expansion contribution and its implications on global ocean volume and regional sea level change indicated as arrows in Figure 1.2. The dark blue arrow between global ocean volume change and regional sea level variability also indicates that these two compartments influence each other which can be seen in Figure 1.1b during $2010 - $ mid 2011 when global mean sea level dropped by $5mm$ due to heavy precipitation in Australia and associated ocean mass redistribution onto the continent (Boening et al., 2012).

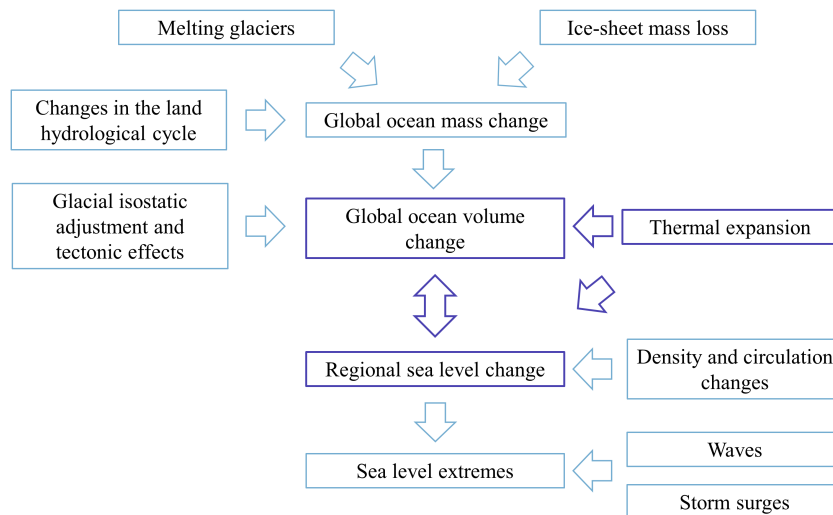FIGURE 1.2: *Schematic of the most important processes and components that contribute to global mean sea level rise. Each outside located box is indicating in which form they affect sea level. Ocean mass changes impact the volume of its basins. Since sea level rise is non-uniform, volume changes are causing regional variability which in turn leads to sea level extremes. Figure adapted from Church et al. (2013).*

The signal of climate change can only be seen when regional sea level exceeds its natural variability and does not return to its normal state for a significant time period, also known as the time of emergence (ToE) (Lyu et al., 2014). Strong natural variability can be observed in regions with strong currents, such as in the North Atlantic Ocean and will, according to climate models, show a late time of emergence. In turn, areas with weaker natural variability such as the tropics will show an earlier ToE. Lyu et al. (2014) states that it takes roughly two to three decades for the total sea level to emerge beyond the natural global sea-level variability. According to models, it is expected that 90% of the global ocean will reach its ToE as early as 2030 (Lyu et al., 2014).

Climate models help in analysing thermal expansion of sea level rise by simulating different states of the climate and investigating phenomena independent of the influence of other contributing factors like melting glaciers and ice sheets as well as changes in the land hydrological cycle. Simulations of 19 climate models by Frölicher et al. (2015) concluded that the Southern Ocean south of 30°S, while occupying 30% of the global surface ocean, accounts for 75% ±23% of heat uptake and storage since the nineteenth century. This thesis will therefore among others focus on how heat uptake, distribution and storage in this area is governed by large scale dynamics of the atmosphere and ocean and how warming influences sea level. A second area of interest is the North Atlantic Ocean where deep water formation during winter months transports large amounts of surface water into depths of 2000 m (Talley, 2000) and which might lead to an associated warming signal and thermosteric expansion of water masses in lower depths.

Chapter 2: Scientific Background

This chapter is intended to give an introduction to the scientific background of total and thermosteric sea level rise. It covers the basic principles and keywords that are necessary to understand the context of this thesis and the following chapters.

2.1 Temperature - Salinity Diagram

The temperature - salinity diagram helps identifying the density of different seawater masses given temperature and salinity values. Density describes the amount of volume a water parcel takes up at a given mass ($\rho = m/V$) and is an integral part in analysing ocean volume changes as a result of temperature differences. Different water masses can have the same density values since it is determined by the interaction of temperature and salt content. Figure 2.1 shows the diagram for a temperature interval of 0 to 25°C and salinity values of $32.5 - 36.5 gkg^{-1}$ as existing in the ocean. The isopycnals or lines of equal density are shown in blue and can either be calculated with the first derivative of pressure from the Gibbs function of sea water $gsw\_rho\_CT\_exact$, which is dependent on salinity S, temperature T and pressure p, or with a polynomial approximation from the same equation. This function for use in Matlab is accessible in the publication by Cooper (2008). For a more detailed description on the toolbox, see Chapter 3.3.

$$\rho = gsw\_rho\_CT\_exact(S_A, \Theta, p_0) = v^{-1} = (\partial g/\partial p)^{-1} \tag{2.1}$$

ρ $\quad \hat{=} \quad$ density of sea water $[kgm^{-3}]$

S_A $\quad \hat{=} \quad$ absolute salinity $[gkg^{-1}]$

Θ $\quad \hat{=} \quad$ conservative temperature $[K]$, see also Section 3.3

p_0 $\quad \hat{=} \quad$ sea surface pressure $[0 dbar]$

v $\quad \hat{=} \quad$ specific volume of seawater $[m^3 kg^{-1}]$

$(\partial g/\partial p)$ $\quad \hat{=} \quad$ partial derivative of Gibbs function with respect to pressure

The isopycnals show the non-linear relation between temperature and salinity in the ocean and can be consulted to distinguish between different water masses. The two arrows indicate how warming of two different water masses by the same temperature change leads to different density values and thus various volumes. The volume of a water parcel eventually determines how much it contributes to sea level rise. Warming 2.5°C cold water by +7°C results in a density change of about $0.001gcm^{-3}$. The same procedure applied to warmer subtropical waters of 17.5°C leads to in higher density loss. The change in density of a sea water parcel is connected to sea level rise by the relation $\Delta V = m/\Delta\rho$. At constant mass m, a water parcel which decreases its density $\Delta\rho$ leads to an increase in volume ΔV. A volumetric expansion eventually causes sea level rise. One of the highest thermosteric sea level trends are therefore expected in tropical water masses where warm water experiences the highest density decrease and as a consequence increases its volume by the highest amounts. As can be seen from Equation 2.1, sea water density is also dependent on salinity. Decreasing the salt content of a water parcel while keeping the temperature constant is also leading to a density loss. However, this thesis is only focusing on density changes due to variations in temperature.
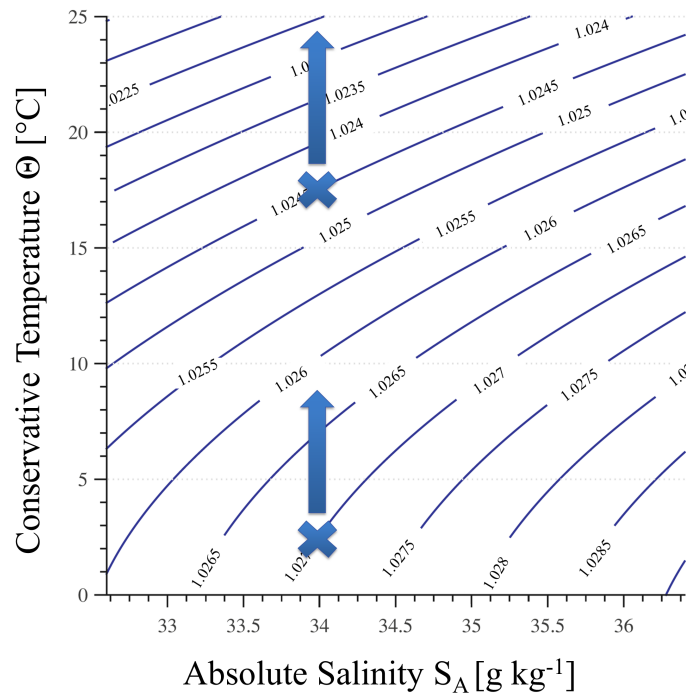

FIGURE 2.1: Temperature − Salinity diagram. Lines of equal density in gcm^{-3}. Figure derived from the Gibbs SeaWater Toolbox (see also Chapter 3.3).

2.2 Ocean Circulation Governing Heat Redistribution

The ocean's Meridional Overturning Circulation (MOC) is a system of surface and deep ocean currents which connects all major ocean basins across longitudes (Schmittner et al., 2013). Upwelling in the Southern Ocean leads to water mass transport from the deep ocean to the surface where they among others exchange heat with the atmosphere. Surface currents such as the Benguela Current in the southeastern or the Gulf Stream in the northwestern Atlantic Ocean transport water masses across the hemisphere to higher latitudes. Cooling of surface water masses in polar regions, sinking due to higher density and subsequent southward flow eventually complete the overturning circulation system. The following Figure 2.2 shows the most important water masses and their general flow pattern in a simplified manner.

- AASW (Antarctic Surface Water)
- SAMW (Subantarctic Mode Water)
- AAIW (Antarctic Intermediate Water)
- UCDW (Upper Circumpolar Deep Water)
- LCDW (Lower Circumpolar Deep Water)
- NADW (North Atlantic Deep Water)
- AABW (Antarctic Bottom Water)
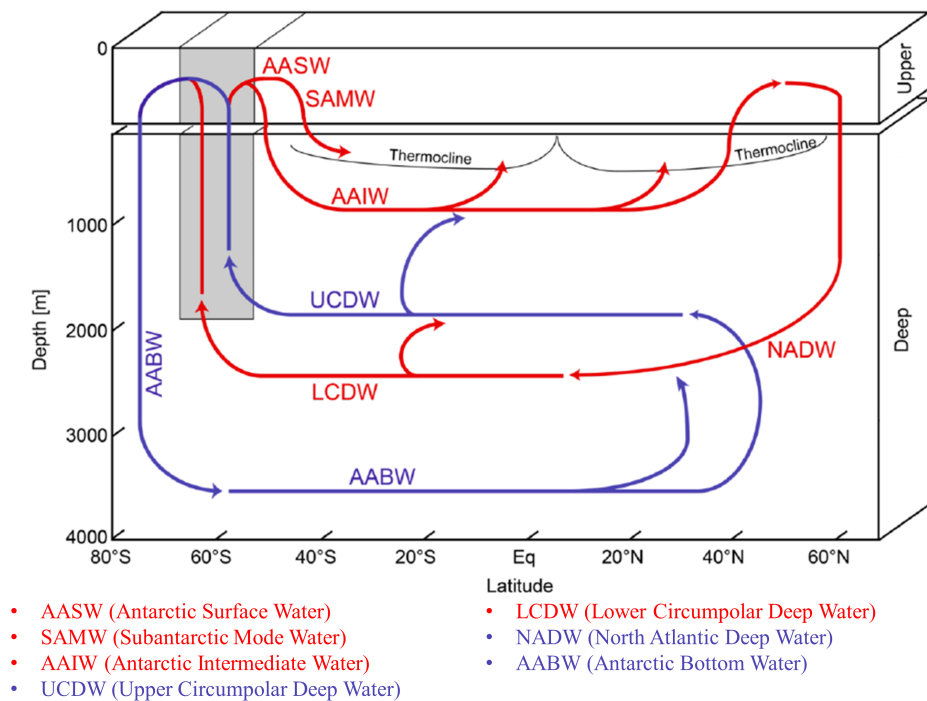
FIGURE 2.2: Schematic of ocean water masses and the meridional overturning circulation. The boundary between upper and deep ocean in this figure is defined to be at 500 m depth. The upper cell in red consists of downwelling in the North Atlantic and upwelling in the Southern Ocean. In the lower cell in blue we have downwelling in the Antarctic and abyssal upwelling in the Indian and Pacific Oceans. The thermocline divides the upper warm mixed water masses from the more stable layers below. It is relatively shallow near the equator due to trade wind-induced turbulent mixing. Figure by Thomas Frölicher at the Federal Institute of Technology Zurich.

The MOC is key in understanding where heat from the atmosphere is taken up, how it is distributed and where it is stored in the ocean. As the warm waters from the tropics flow north, they loose heat by cooling. If heat is only taken up by the surface layers, as it is happening in the tropics, it can easily be released back into the atmosphere as a result of high evaporation rates. Permanent storage occurs dominantly where water masses are transported into the ocean's interior and heat exchange with the atmosphere is prevented.

2.2.1 Southern Ocean Circulation

The Southern Ocean is dominated by the Antarctic Circumpolar Current (ACC). It is the strongest ocean current and the only one which spans around the globe unhindered Smith et al. (2013). The eastward flow is driven by strong westerly winds (Smith et al., 2013) pushing water masses to the side and driving upwelling of among others North Atlantic Deep Water (NADW) to the surface (see the northern section of Figure 2.3). The upwelled water is cold and can absorb large amounts of heat from the atmosphere (Morrison et al., 2015).

The Coriolis force, i.e. a force that acts perpendicular to the direction of motion and to the axis of rotation on a rotating sphere (Gill, 1982), deflects the wind driven ocean current in the uppermost layers to the left. The resulting net transport of Antarctic Surface Water (AASW) is deviated by 90° from the wind direction (Ekman, 1905). Heat uptake is substantial in this upwelling region as a result of the constant northward transport and subsequent replenishment of cold deep water from below. At around 50°S the AASW reaches the Antarctic Convergence zone where there is a strong temperature gradient between cold Antarctic water and warmer Subantarctic water masses. The AASW with higher density than the Subantarctic water to the north begins to sink and turns into Antarctic Intermediate Water (AAIW). According to Gruber et al. (2009), it reaches depths of up to 800 m.

Winds blowing parallel to the Antarctic coast in eastward direction also drive coastal upwelling similar to the processes in the more northward situated ACC (see the southern section of Figure 2.3). Deep water masses reach the surface where they take up heat. Cooling and density increase through sea ice build-up leads to Antarctic Bottom Water (AABW) formation (Kerr et al., 2012). This water mass is one of the most dense in the World, sinks to the abyssal depths and out into the Indian, Pacific and Atlantic basins.
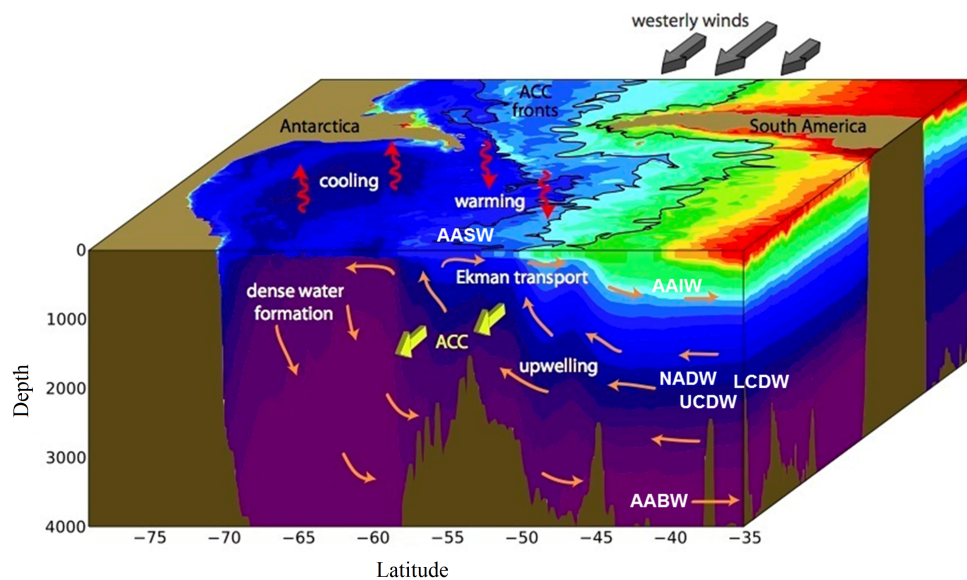
FIGURE 2.3: Dynamics in the Southern Ocean showing where deep and cool water masses get in contact with the atmosphere and take up heat. The cross-section shows Westerlies which drive the ACC, upwelling of deep water masses to the surface, the subsequent Ekman transport as AASW and subduction as AAIW in the Subtropics. Upwelling induced by coastal winds also brings deep water to the surface. These water masses cool and condense as sea-ice forms which leads to AABW formation and transport to abyssal depths. Colouring is an indicator for the temperature where cold water masses represent purple and blue areas whereas warmer water masses are shown in green, yellow and red. Figure taken from (Morrison et al., 2015).

2.2.2   North Atlantic Ocean Circulation

Alongside the region of ACC upwelling, the North Atlantic is important in transporting heat into depths of 2000 m (Talley, 2000), much lower than the heat storage by AAIW in the southern Subtropics. The North Atlantic Current (NAC) as an extension of the Gulf Stream transports warm and salinity rich waters towards the higher latitudes (see the following Figure 2.4). North Atlantic Deep Water (NADW) formation occurs in three locations; in the Greenland, Labrador and Irminger Seas (Talley, 2000) indicated as stars in Figure 2.4. In these three areas, warm water masses from the North Atlantic Current are transformed into cool and dense water especially during wintertime and sink through diapycnal mixing, i.e. mixing across density surfaces (Umlauf and Burchard, 2011), open ocean convection (Moore et al., 2015) or mixing adjacent to steep topography (Spall and Pickart, 2001).
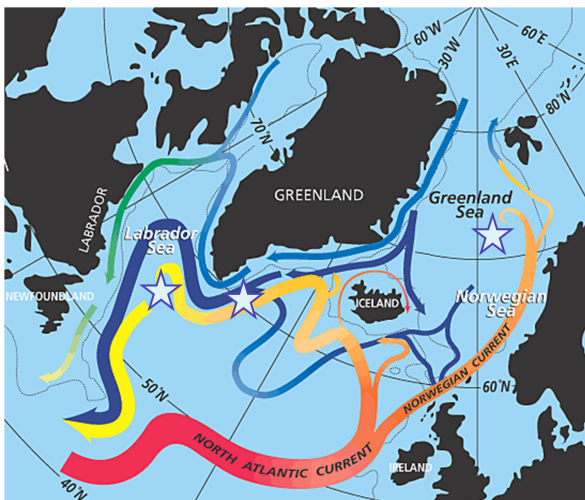

FIGURE 2.4: Circulation patterns in the North Atlantic Ocean. The three deep water formation sites are indicated as stars in the Greenland, Labrador and Irminger Seas. The Greenland and Norwegian Seas are often referred to as the Nordic Seas and are the main connection between the Arctic and the Atlantic Oceans. The colour shading indicates the temperature of the individual ocean currents with blue and green representing values in the range of $[-2°$ to $3°C]$ and yellow $-$ red standing for $[3°$ to $12°C]$. Illustration by Jack Cook at the Woods Hole Oceanographic Institution.

Strong cold and dry winds from the North American continent and around the southern coast of Greenland positively impact surface heat loss in the Labrador and Irminger Seas (Moore et al., 2014, Pickart et al., 2003). Deepwater formation in the Nordic Seas is impacted by convection in the Greenland and Iceland gyres (Moore et al., 2015) as well as mixing with dense southward flowing brine water from the Arctic Ocean (Aagaard et al., 1991) (a gyre represents a large system of circular ocean currents formed by winds and

the Coriolis force while brine water stands for a water mass with a high salinity content, as is occurring after sea-ice formation in the Arctic Ocean). Out of these three locations, the cold and dense NADW water masses flow south mainly on the western boundary of the Atlantic subpolar gyre (Langehaug et al., 2012). This cyclonic or clock-wise turning system takes up the newly formed dense water masses on its northern lower limb and pushes them into the subtropics (Langehaug et al., 2012).

NADW formation is not always constant and depends on how much heat the water masses loose. Less heat loss can be a result of short-term natural variabiliy or long-term climate change due to increased radiative forcing. Warmer water masses don't become as dense as they would in colder conditions, however they can still sink into the ocean interior and show up as a positive signal. When warmer conditions are long-lasting, the positive heat anomaly in the deep ocean is greater and remains for longer time periods.

Chapter 3: Data and Methods

This chapter describes the origin of the data sets used in this thesis and which equations were used to calculate temperature, thermosteric sea level and heat content changes.

3.1   Observational Data Sets

The global mean sea surface height and regional sea level trend map data from the four satellites Topex/Poseidon, Jason-1 and Jason-2 for $1993 - 2016$ is provided by the National Oceanic and Atmospheric Administration (NOAA) Laboratory for Satellite Altimetry. For this thesis, the data set with removed seasonal signals is chosen and reduced to mean annual values. It is available through the following link:

http://www.star.nesdis.noaa.gov/sod/lsa/SeaLevelRise/LSA_SLR_timeseries_global.php

The observed ocean heat content change data for $0 - 700$ m (for the time period $1993 - 2015$) and $0 - 2000$ m ($2005 - 2015$) is based on ocean float data from the Argo program and is obtained from the NOAA National Centers For Environmental Information: https://www.nodc.noaa.gov/OC5/3M_HEAT_CONTENT/, (Levitus et al., 2012).

These observational data sets on the global and regional scale will be compared to the model data to examine if the model calculations are able to reproduce real values.

3.2   Model Data Sets

Climate models help in understanding sea level rise and its underlying contributing processes independently of each other. In this section, the influence of temperature change on sea level rise and the anomaly in oceanic heat content change during $1993 - 2016$ will be calculated with the atmosphere-ocean general circulation model Community Climate System Model 4 (CCSM4) output. The analysis is based on a combined historical + future projection simulation run. The historical simulation run includes observed values of greenhouse gas (GHG) concentration while the future projection named rcp85 defines a

radiative forcing of +8.5W/m² in 2100 and interpolates the GHG concentration to match this boundary condition.

The CCSM4 is a coupled climate model consisting of four separate models simultaneously simulating the Earth's atmosphere, land surface, sea-ice and ocean while a central coupler combining the different parts (Vertenstein et al., 2011). The model allows simulations for past, present and future climate states under different radiative forcing conditions. This model is also part of the Coupled Model Intercomparison Project 5 (CMIP5) and was used to assess the state of the climate system for the Intergovernmental Panel on Climate Change's (IPCC) 5th Assessment Report.

The CCSM4 model output data is downloaded from the Institute of Atmospheric and Climate Science at the Swiss Federal Institute of Technology in Zurich. The following variables from the model are needed for the calculations in each grid cell: *so* (salinity), *thetao* (potential temperature), *volcello* (volume), *areacello* (area), *lev_bnds* (depth), *deptho* (total depth of the ocean), *lon* (longitudinal values) and *lat* (latitudinal values for mapping procedures). The variable $REGION\_MASK$ (a map array defining boundaries between ocean basins) is used from an earlier iteration of the same model and still applicable. Since historical integrations end in 2005, it has been decided to use rcp85 data for the remaining years of the time series.

3.2.1 Model Drift Correction

Most climate models including CCSM4 experience long-term changes without the influence of radiative forcing (Gupta et al., 2013). Thus, a pre-industrial control run simulation is done over an extended period of time where the system receives time to adapt to a state close to the representation of equilibrium (Gupta et al., 2013) and where no long-term trends are visible. From there, the historical simulation is started. Since the control simulation is not in equilibrium and also displays a drift during the historical + rcp85 simulations, this deviation has to be removed from the analysis.

3.3   Calculation of Temperature Change

For the conversion of potential temperature θ into conservative temperature Θ to use in the calculation of the thermal expansion coefficient α and the calculation of sea water density ρ, functions from the Gibbs-SeaWater (GSW) Oceanographic Toolbox are used. All three functions are based on the Gibbs function $g(S, T, p)$ which describes the equation of state for seawater in dependence of salinity S, temperature T and pressure p. Due to its complexity, it has been decided not to include the function here. The full Gibbs function can be accessed either in the publication Thermodynamic Properties of Seawater by Cooper (2008) or in the GSW Toolbox manual: http://www.teos-10.org/pubs/TEOS-10_Manual.pdf. The open-source toolbox is available from the Thermodynamic Equation of Seawater − 2010 website: http://www.teos-10.org/software.htm, (McDougall et al., 2009).

Potential temperature values in each ocean grid cell for the specified time series first get converted into conservative temperature. Conservative and potential temperature values in oceanic conditions are very similar because the same concept is involved in their definitions (McDougall and Barker, 2011). Potential temperature is obtained when lifting a sample of seawater in an adiabatic and isohaline way, i.e. withouth exchange of heat and salinity with the surrounding water, from the depth to the surface. Potential enthalpy (the thermodynamic quantity for the amount of heat) is derived the same way. Conservative temperature is simply defined as the potential enthalpy divided by the constant heat capacity c_p (Jackett et al., 2006). McDougall and Barker (2011) states that conservative temperature represents the heat content of seawater much more accurately and thus is used in the calculations.

The conversion of potential into conservative temperature is being done with the function *gsw_CT_from_pt* (represented in Equation 3.1). Conservative temperature in each grid cell is dependent on absolute salinity S_A, potential temperature θ and pressure at sea water surface p_0 which for the entire thesis is set at zero.

$$\Theta_i = gsw\_CT\_from\_pt(S_{A_{1993}}, \theta_i, p_0) = \frac{g(S_{A_{1993}}, \theta_i, p_0) - (T_0 + \theta_i)\,(\partial g/\partial \theta_i)}{c_p} \quad (3.1)$$

Θ_i	$\hat{=}$	mean annual conservative temperature in year i $[K]$
$S_{A_{1993}}$	$\hat{=}$	absolute salinity in year 1993 $[gkg^{-1}]$
θ_i	$\hat{=}$	mean annual potential temperature in year i $[K]$
p_0	$\hat{=}$	ocean pressure at sea surface $[0dbar]$
$g(S_{A_{1993}}, \theta_i, p_0)$	$\hat{=}$	Gibbs function dependent on $S_{A_{1993}}, \theta_i$ and p_0
T_0	$\hat{=}$	Celsius zero point $[273.15K]$
$(\partial g/\partial \theta_i)$	$\hat{=}$	first partial derivative of Gibbs function with respect to θ_i
c_p	$\hat{=}$	specific heat capacity $[3.99 * 10^3 Jkg^{-1}K^{-1}]$

To isolate the expansion in each grid cell due to temperature change, salinity has been defined as the mean annual 1993 values throughout the time period.

Figure 3.1 shows how the conservative temperature difference in each grid cell has been determined. A linear trend is fitted through the 24 mean annual values. The conservative temperature change $\Delta\Theta$ is defined to be the difference between the linear trend values of 1993 and 2016. Additionally, the model drift linear trend is subtracted from the historical + rcp85 trend.

$$\Delta\Theta = (ts(\Theta_{2016}) - ts(\Theta_{1993})) \quad (3.2)$$

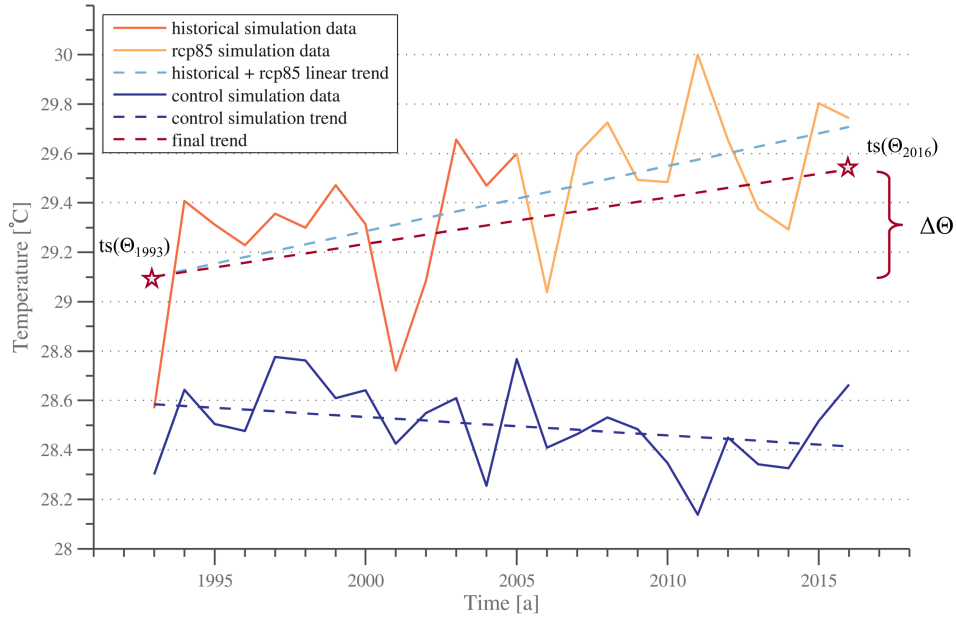|		
$\Delta\Theta$	$\hat{=}$	conservative temperature trend difference $[K]$
$ts(\Theta_i)$	$\hat{=}$	conservative temperature trend value in year i $[K]$

FIGURE 3.1: Modelled mean annual conservative temperatures and associated trends in grid cell [1, 140, 190] near Fiji in the Pacific Ocean. The historical + rcp85 annual values are shown in orange colouring and their associated trend as a dashed line in light blue. The control run mean annual values and their trend are in dark blue. To isolate the model drift, the control simulation trend difference is subtracted from the historical + rcp85 linear trend which results in the dark red trend. The final temperature difference for this time period $\Delta\Theta$ is defined as the difference in initial and final trend values indicated as stars.

3.4 Calculation of Thermal Expansion

The thermal expansion coefficient α, i.e. the degree of expansion per change in temperature, is calculated with the GSW Toolbox function *gsw_alpha_CT_exact* (represented in Equation 3.3) dependent on initial absolute salinity $S_{A_{1993}}$, initial conservative temperature from the calculated trend $ts(\Theta_{1993})$ and sea surface pressure p_0.

$$\alpha_{1993} = gsw\_alpha\_CT\_exact(S_{A_{1993}}, ts(\Theta_{1993}), p_0) = v^{-1}(\partial v / \partial \Theta_{1993}) \tag{3.3}$$

$\alpha_{1993} \quad \hat{=} \quad$ annual mean thermal expansion coefficient in year 1993 $[K^{-1}]$

$v \qquad \hat{=} \quad$ specific volume of seawater $\rightarrow$ see also Equation 2.1

For each grid cell, the total sea surface height change over the 25-year period is determined by dividing the total volume change ($V_0 \alpha \Delta \Theta$) with its area A. This equation is obtained from Tipler and Mosca (2007).

$$\Delta h = \frac{V_0 \alpha_{1993} \Delta \Theta}{A} \tag{3.4}$$

$$
\begin{aligned}
\Delta h &\;\hat{=}\; \text{thermosteric height anomaly } [m] \\
V_0 &\;\hat{=}\; \text{initial grid cell volume } [m^3] \\
A &\;\hat{=}\; \text{grid cell area } [m^2]
\end{aligned}
$$

3.5 Calculation of Heat Anomaly

The initial and final seawater density values are calculated with the GSW Toolbox function $gsw\_rho\_CT\_exact$ in each grid cell and are dependent on initial absolute salinity $S_{A_{1993}}$, conservative temperature from the calculated trend $ts(\Theta_i)$ and sea surface pressure p_0.

$$\rho_i = gsw\_rho\_CT\_exact(S_{A_{1993}}, \Theta_i, p_0) = v^{-1} = (\partial g/\partial p)^{-1} \tag{3.5}$$

$$\rho_i \;\hat{=}\; \text{mean annual potential density in year } i \; [kgm^{-3}] \rightarrow \text{see also Equation 2.1}$$

The total heat content anomaly is the result of the difference between the initial and final heat content of the evaluated time period. The equation is derived from Fourier's law and the conservation of energy and among others stated in the book by Cannon (1984).

$$Q_{1993} = \rho_{1993} c_p V_0 \Theta_{1993} \tag{3.6}$$

$$Q_{2016} = \rho_{2016} c_p V_0 (\Theta_{1993} + \Delta\Theta) \tag{3.7}$$

$$\Delta Q = Q_{1992} - Q_{2016} \tag{3.8}$$

$$
\begin{aligned}
Q_i &\mathrel{\hat{=}} \text{ heat content in year } i \ [J] \\
c_p &\mathrel{\hat{=}} \text{ specific heat capacity} \rightarrow \text{see also Equation 3.1} \\
\Delta Q &\mathrel{\hat{=}} \text{ heat content anomaly } [J]
\end{aligned}
$$

The model's ocean grid cell volume V_0 is constant, but the volume change is implicit in the density difference. This can be seen in Equation 2.1

Chapter 4:   Results and Discussion

This chapter will present the calculated results from the thermal expansion trend, the temperature trend and the heat content anomaly calculations on the global and on the regional scale. Comparisons with observed and published data check the correctness of the calculation and the model's ability to simulate this specific part of the Earth's climate system.

4.1   Thermosteric Contribution

The observed global mean annual sea level rise trend from the beginning of 1993 up to the first quarter of 2016 is 2.9 [2.5 to 3.3] mm/year (Figure 4.1). In the model, the global mean annual thermosteric trend calculated with Equation 3.4 is 1.5 mm/year and explains 53 % of the global mean trend for this time period as can be seen in Figure 4.1. When consulting Figure 1.2, the remaining contributors in the model might be due to the flux of freshwater from melting glaciers and ice-sheets and from changes in the land hydrological cycle. It is assumed that glacial isostatic adjustment, tectonic effects and density and circulation changes play a minor role in global mean sea level rise for this time period.

When comparing the calculated thermosteric trend with the CMIP5 ensemble mean results published in the IPCC Fifth Assessment Report, the calculated trend lies within the 95% confidence interval for observed and modelled trends (see Table 4.1) although the report lists values for a different time period. A comparison with observed data from satellite altimetry shows that mean model trends slightly overestimate observed data. The thermosteric trends calculated from the CMIP5 models are viable and comparable to observation-derived trends and their uncertainty intervals from the IPCC Fourth and Fifth Assessment Report as well as from Cazenave and Llovel (2010).

This comparison is biased due to data from different time periods but still made under the assumption that the different trends extrapolated until 2016 would not have changed dramatically. The consistency of these estimates could also indicate that thermal expansion for this time period is to a certain extent linear.
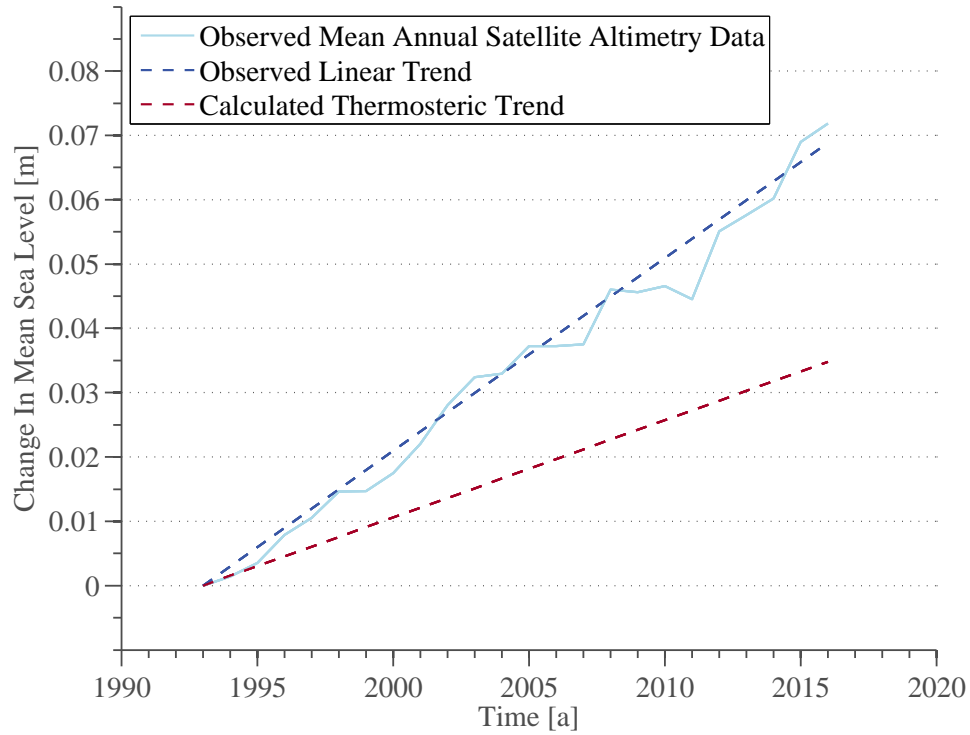
FIGURE 4.1: Observed global mean sea level in light blue, its calculated mean annual trend as a dashed line in darker blue and the modelled thermosteric sea level trend as a dashed red line for the time period $1993 - 2016$. The observed mean annual trend indicates a sea level rise of 2.9 [2.5 to 3.3] mm/year and the modelled thermal expansion trend reveals a 1.5 mm/year contribution.

Trend from	Time Period	Data derived from	Value
Calculations in eq. 3.1 − 3.4	$1993 - 2016$	CCSM4 model	1.5 mm/year
IPCC AR5 (Church et al., 2013)	$1993 - 2010$	25 CMIP5 models	1.49 [0.97 to 2.02] mm/year
IPCC AR4 (Antonov et al., 2005)	$1993 - 2003$	Observations	1.23 [1.03 to 1.43] mm/year
IPCC AR5 (Church et al., 2013)	$1993 - 2010$	Observations	1.1 [0.8 to 1.3] mm/year
Cazenave and Llovel (2010)	$1993 - 2007$	Observations	1.0 [0.7 to 1.3] mm/year

TABLE 4.1: Comparison of observed and modelled global mean thermosteric trends from the IPCC 4th and 5th Assessment Report and from Cazenave and Llovel (2010). The CCSM4 model used in this thesis is also part of the CMIP5 project. Values in square brackets represent the 95% confidence intervals.

The following trend maps in Figure 4.2 represent observed and modelled thermosteric sea level rise and its spatial distribution of Figure 4.1. From this is apparent that high sea level rise does not per se result in high thermosteric trend values. The previously introduced temperature dependence of water volume and the associated thermosteric sea level rise will now be discussed in the next sections.
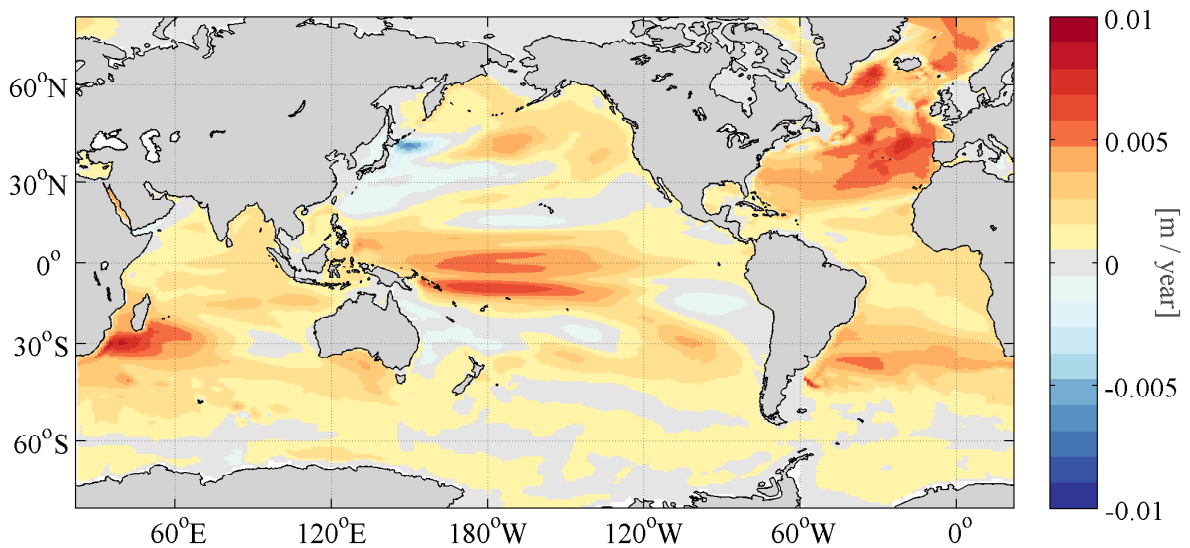
a)
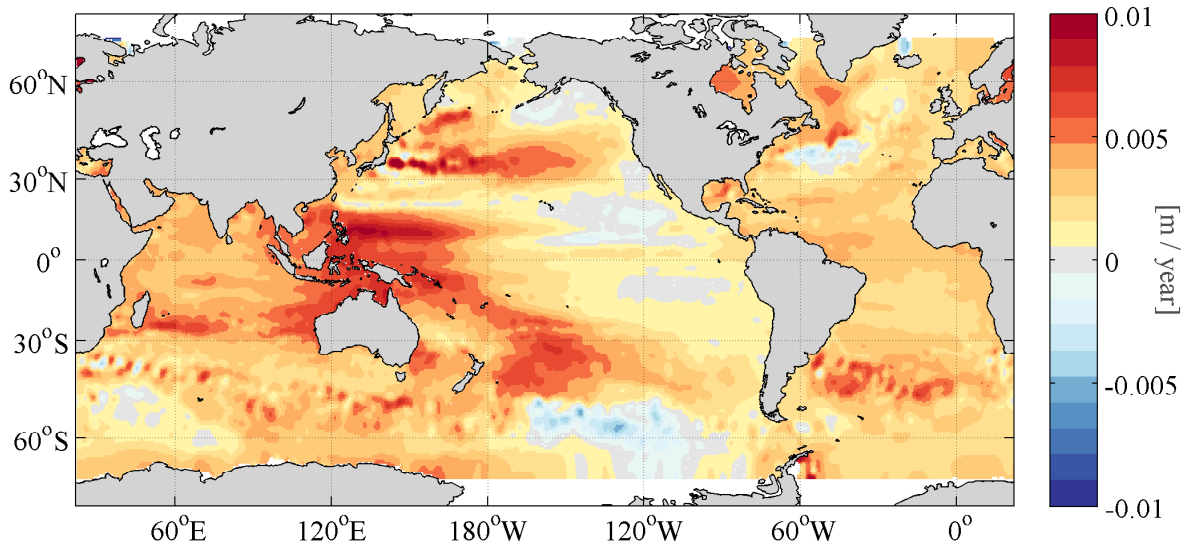
b)

FIGURE 4.2: In a) the linear trend in observed total sea level rise from $1993 - 2016$. The white space north of $70°$ latitude is a result of no data points. In b) the modelled thermosteric trend as calculated with Equation 3.4 for the same time period.

4.2   Temperature Trend

The modelled ocean water temperature trend map calculated by using Equation 3.2 shows a positive trend in most regions (Figure 4.3). Most of the warming occurs in the Northern Hemisphere, especially in the Atlantic and Arctic Oceans. Pithan and Mauritsen (2014) state that one of the major contributors to the high temperature trend in CMIP5 models during the last 30 years is the surface-albedo feedback. As sea-ice and snow retreats, it leaves the ocean's dark surface behind. These newly uncovered areas have a higher surface absorption rate and therefore lead to increased temperatures.
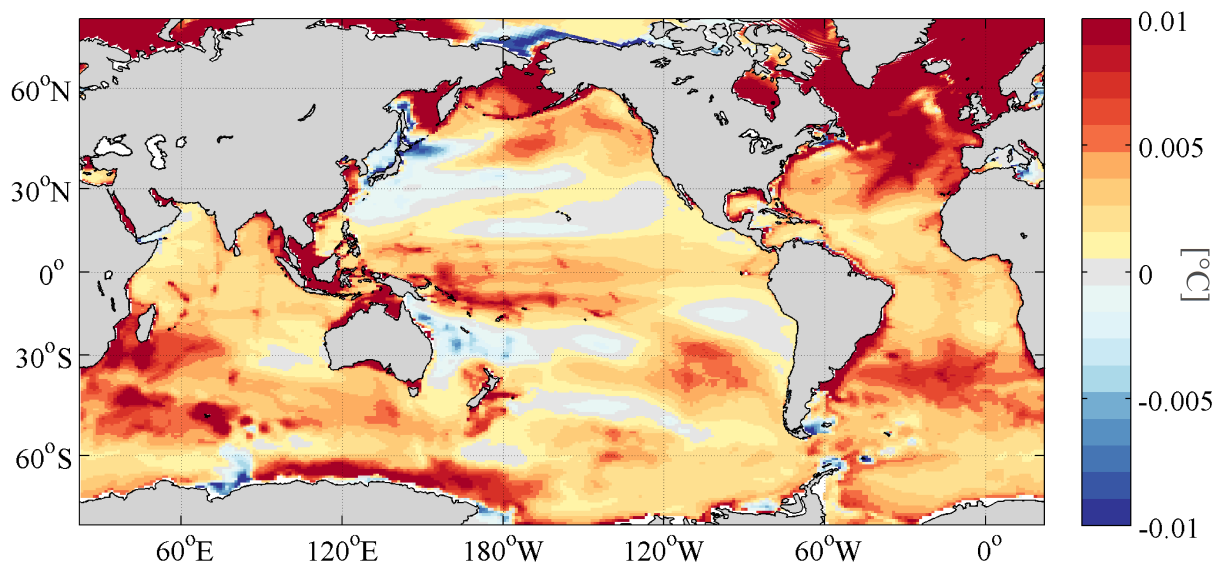
FIGURE 4.3: Modelled depth averaged temperature trend for the entire water column for $1993 - 2016$. The saturated colour bar indicates there are values higher than $0.01°C/year$.

The temperature trend in the polar regions of the Southern Hemisphere is less pronounced than in the Arctic. Nonetheless, there is still a considerable large trend near the Antarctic coast between $70°E - 180°W$. This might be due to a decreasing strength of the ACC which leads to warmer ocean temperatures or the result of increased sea ice extent. A larger area covered in sea-ice results in a higher surface albedo feedback and thus smaller temperature trend (Sinclair et al., 2012). Therefore, natural variability in sea-ice formation can have large impacts in regards to thermosteric sea level rise but is not further adressed in this thesis. The Temperature-Salinity Diagram in Section 2.1 also explains

that a high temperature trend in cold polar water masses has a smaller impact on density and thus volume change than the same in tropical conditions. Furthermore, the shallow shelf regions around Antarctica, despite their large temperature trends, only expand little as a result of the volume dependence of thermal expansion (see also Equation 3.4). The same is true for the Arctic Ocean which largely covers shallow shelf regions.

Off the southwestern coast of Africa and South America, thermosteric sea level rise may contribute a substantial amount to the observed total. There, water masses experience a high temperature trend and a high volume change (Figures 4.3 and 4.2b). Sea level rise in those two areas might be fully explained by thermal expansion while the other contributors from Figure 1.2 play a minor role or are of opposite signs so they cancel each other out.

The large positive thermal expansion trend in most areas of the Northern Atlantic could be viewed as a result of its large temperature trends. Observational data analysed in Carton and Santorelli (2008) shows a subtropical Atlantic temperature trend of twice the global average since the 1960s. High heat uptake and subsequent deepwater formation could lead to increased rates of temperature in deeper parts of the ocean which in turn affect the thermosteric trend.

A higher than average modelled temperature trend is also apparent in the western equatorial Pacific. There, high initial temperatures combined with high temperature trend values lead to substantial density losses in these water masses and therefore the highest thermal expansion trends. Additionally, this anomaly limited to the western Pacific Ocean is also likely impacted by an increase in Pacific trade wind intensity (Figure 4.2b). An asymmetry in El Niño − La Niña strength for 14 coupled models from the CMIP5 project has been evaluated in Zhang and Sun (2014) . A La Niña event is representative of increased eastward blowing trade winds, a warm western equatorial Pacific and increased upwelling of deep water masses in the eastern equatorial Pacific while an El Niño event is the opposite state of the El Niño-Southern Oscillation (ENSO). Zhang and Sun (2014) state that it is common for models to simulate different strengths for the mean ENSO states. In general, Zhang and Sun (2014) showed that most models simulate weaker El Niño events due to both weaker sea surface temperature anomalies and less pronounced

precipitation anomalies over the eastern Pacific relative to its western side. Also according to Zhang and Sun (2014), the modelled strength of the La Niña events are comparable to observations. This imbalance between weaker simulated El-Niño and normal La Niña phases of the ENSO may therefore lead to the higher temperature trends in the western equatorial Pacific of Figures 4.3 and 4.2b).

High heat uptake and warming of water masses as mentioned for the Atlantic Ocean may lead to their expansion in the deep ocean and will now be discussed in detail.

4.3   Heat Content

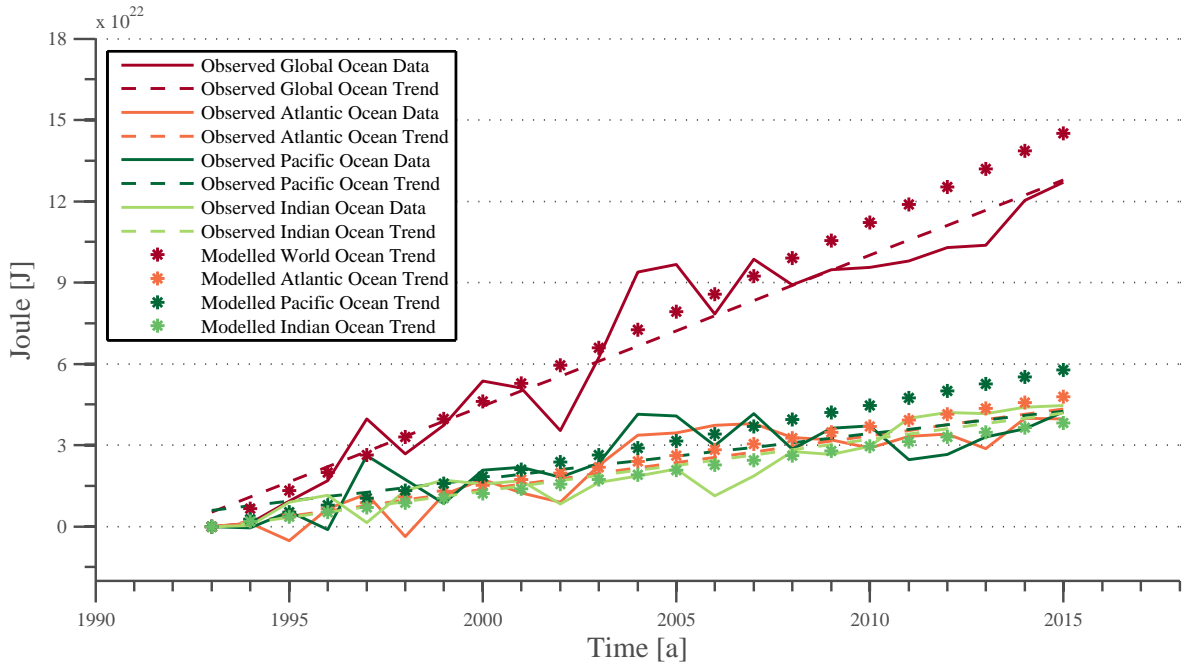### 4.3.1   Observed and Modelled Ocean Heat Content Changes

The calculations in this thesis have been done for the last 24 years which allows for comparison with observed data sets from Argo floats. Figures 4.4a and 4.4b show a comparison of observed and modelled heat content trends during $1993 - 2015$ for the upper 700 m and during $2005 - 2015$ for the upper 2000 m. To arrive at the best possible comparison, the following considerations are made:

- To limit the effect of short − term or interannual variability, a linear trend approximation is considered the best for both observed and modelled heat content.

- The modelled calculations are done until the end of 2016 whereas observational data ends in March 2016. It is assumed that the linear trend for $1993 - 2015$ and $1993 - 2016$ is the same since earlier calculation of the thermosteric trend for the two time periods $1992 - 2016$ and $1993 - 2016$ resulted in the same outcome.

- Modelled values from the Greenland Sea and the Arctic Ocean are included in the Atlantic Ocean to match the observational data set.

- The observed data set defines the borders between the three major as follows: The Indian Ocean covers the area between $22°E - 145°E$ including the Southern Ocean. The boundary between Indian and Pacific Ocean follows the $145°E$ latitude from

Antarctica to Australia and then to the northern Indonesian Isles to Malaysia. On the northern border, the Pacific is separated from the Arctic Ocean at the Bering Strait. The Atlantic Ocean is defined to cover the remaining parts of the ocean basin including the Arctic Ocean. For the comparison, the boundaries in the model have been redefined to match those of the observed data set. The described boundaries can also be seen in Map 4.7a as dashed and solid lines. Since this map also shows boundaries defined for later analysis, only the here mentioned borders should be considered.

- Smaller basins such as the Baltic, Mediterranean and Red Seas are not considered in the modelled trend since it is assumed they do not influence the comparison on the global scale.

- Due to the vertical resolution of the model, values down to 747 m and down to 2077 m instead of 700 m and 2000 m as in the observations were used.
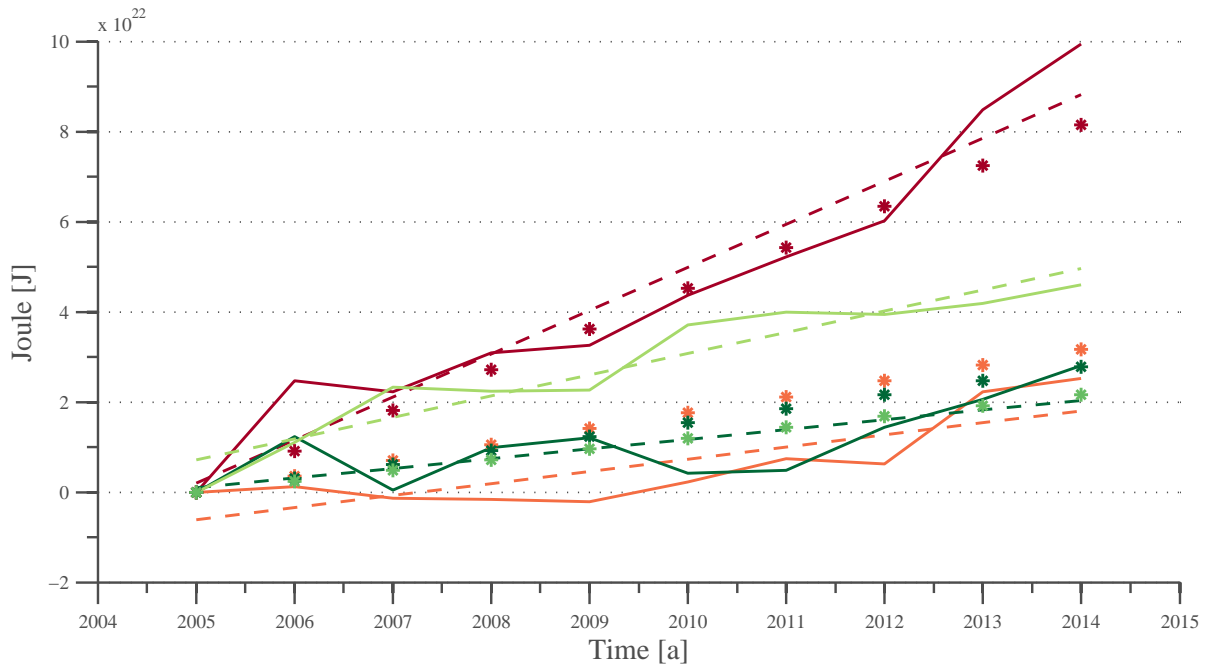
a) upper 700 m

b) upper 2000 m

FIGURE 4.4: Comparison of global observed and modelled ocean heat content in the upper a) 700 m and b) 2000 m. The comparison for b) is from 2005 onwards and thus only includes rcp85 data from the model. The legend box in a) applies applies for both Subfigures.

The difference between the observed and the modelled global ocean trend in Figure 4.4a is 18%. Observational trends for the three basins in the 700 m comparison are nearly identical, the modelled trends however differ substantially. The difference between observed and modelled trends may be explained by varying influences of volcanic, solar and aerosol forcing which are all active in the CCSM4 historical simulation (National Center for Atmospheric Research). From 2005 onwards, an increased rate of radiative forcing is applied to the model's climate system by the rcp85 scenario and which might deviate from observed forcing rates and natural variability at this time. The observed trend shows higher heat storage in the Pacific Ocean than what the model calculates. This might be due to a lower than average Southern Ocean storage in CCSM4 and will be discussed in detail in a later section.

The same comparison for the 2000 m ocean from 2005 onwards illustrates a smaller deviation between observed and modelled global ocean trend (see Figure 4.4b). However, the difference between the individual basin trends is generally bigger than in the 700 m ocean comparison of Figure 4.4a. The biggest difference between observed and modelled trends is found in the Indian Ocean. There, observations show roughly double the amount of heat storage in comparison with the model calculations. Argo float records in this time period showed that the enhanced Indian Ocean heat storage is due to increased ocean circulation through the Indonesian throughflow from the Pacific Ocean where heat uptake took place (Lee et al., 2015). Therefore, the Indian Ocean could potentially have a bigger impact on climate variability than what the model simulates.

Concluding from both Figure 4.4a and 4.4b, ocean heat storage for the historical + rcp85 calculation overestimates observed global 700 m heat storage and the early stages of the rcp85 simulation underestimate global 2000 m heat storage. It should also be noticed that all CMIP5 models simulate slightly more Southern Hemisphere ocean heat storage due to initial filling up of data-sparse regions of the ocean with estimates (Durack et al., 2014). A comparison of modelled and observed deep ocean values below 2000 m cannot be made due to scarce data (Roemmich et al., 2009).

4.3.2   Anomaly on the Global Scale

From now on, statements on heat anomalies, when not indicated as observational data, are referring to the calculated model output.

A total of 2.24×10^{23} Joule has been taken up and subsequently stored by the ocean since 1993. As discussed in the comparison above, this is approximately as was observed in this time period. On a global scale, about ²/₃ is stored in the upper 747 m and only ¹/₃ reaches lower depths between 747 m and 5500 m. The definition of the upper and deep ocean applies from now on to all references of these two layers. Figure 4.5 represents the modelled cumulative vertical heat storage for the global ocean and the individual basins. Table 4.2 shows the integrated total, upper and deep ocean values for the different basins.
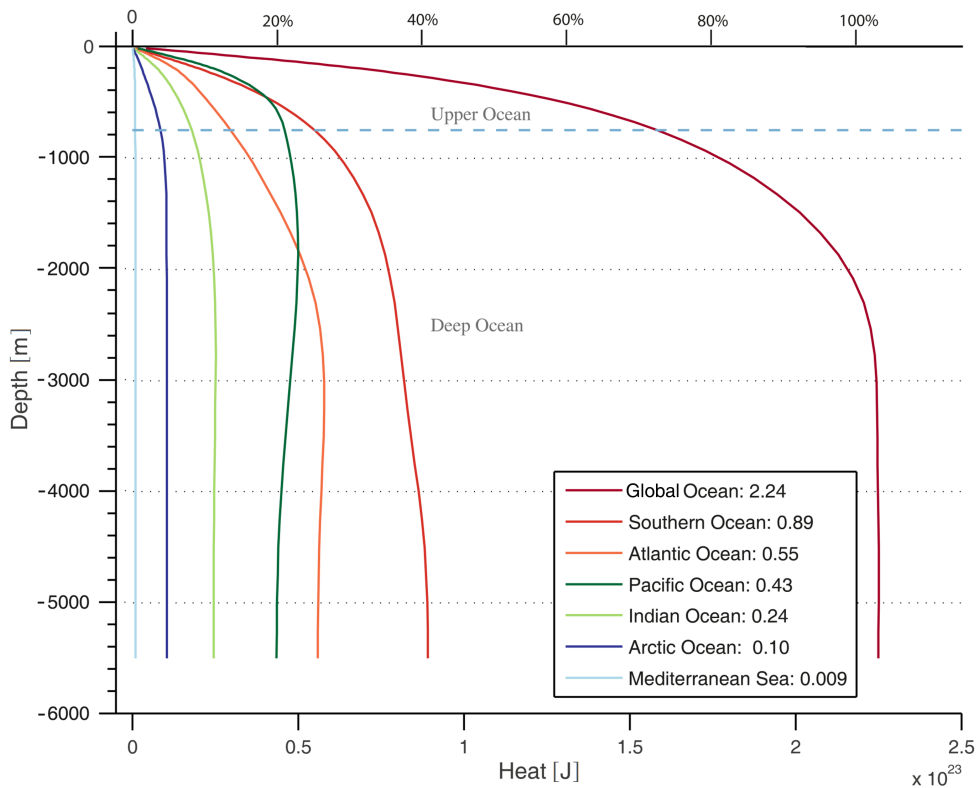
FIGURE 4.5: Modelled cumulative ocean heat content change between $1993 - 2016$. Values in the legend indicate total heat uptake for this time period in 10^{23} Joule. Rounding uncertainties explain the difference of 0.021×10^{23} Joules between the sum of the individual basins and the total amount stored. The Arctic Ocean includes values from the Greenland Sea while the Labrador Sea is included in the Atlantic Ocean. The boundary between upper and deep ocean is defined to be at 747 m depth. The percentage scale on the top indicates heat storage of an individual basin relative to the global ocean.

Ocean	Contribution to Total	Upper Ocean	Deep Ocean
Global Ocean	2.24 (100%)	1.58 (70.6%)	0.66 (29.4%)
Southern Ocean	0.89 (39.7%)	0.54 (60.6%)	0.35 (39.4%)
Atlantic Ocean	0.55 (24.5%)	0.29 (52.7%)	0.26 (47.3%)
↳ North Atlantic $40-80°$N	0.27 (12.0%)	0.14 (51.8%)	0.13 (48.2%)
Pacific Ocean	0.43 (19.2%)	0.45 (104%)	-0.02 (-4%)
Indian Ocean	0.24 (10.5%)	0.17 (70.8%)	0.07 (29.2%)
Arctic Ocean	0.10 (4.4%)	0.08 (80.0%)	0.02 (20.0%)
Mediterranean Sea	0.009 (0.3%)	0.008 (88.8%)	0.001 (11.2%)

TABLE 4.2: Vertical heat distribution in individual ocean basins. In the second column, each basin's total heat storage and the relative percentage to the global ocean are listed. The third and fourth column contain values how much each basin stores in the upper ocean and the deep ocean. The percentage values in the last two columns indicate how much of the basin's heat is stored in each of the two layers. All values are in order 10^{23} Joule.

Storage below 3000 m depth in the global ocean is minimal. For the heat to reach such deep layers, it must be either advected, diffused or vertically mixed down (Gregory, 2000). The only basin which shows a heat anomaly, although not a considerable signal, in the depths lower than 3000 m is the Atlantic Ocean. All other basins accumulate their heat at shallower depths. Furthermore, from the individual basins, it can be seen that the Southern Ocean stores the most heat. In the model, this basin has been defined to cover the area south of 34°S, i.e. the full area extent south of the Cape of Good Hope in Africa. This area already covers a substantial amount of the modelled ocean ($0.95 \times 10^{14}m^2$ or roughly 26%), yet it stores a larger than expected amount of heat, i.e. ~40% of the global anomaly. The ensemble mean of 20 CMIP5 models analysed by Frölicher et al. (2015) shows that the Southern Ocean south of 30°S accounts for 75% ± 22% of the global heat storage since the pre-industrial time. Therefore, the Southern Ocean in models is more important than what the CCSM4 model suggests while also keeping in mind that the CCSM4 Southern Ocean is 4° latitudes smaller than the one defined by Frölicher et al. (2015).

Not only the Southern Ocean plays an integral role in heat storage, the Atlantic Ocean anomaly is also noticeable. This basin, while covering half the area extent of the Pacific Ocean, not only stores more heat but also does so by accumulation in the deep ocean (see the North Atlantic in Figure 4.6a). Out of the global stored 0.66×10^{23}J in the deep ocean, 40% is concentrated in the Atlantic area despite its basin only covering 17.5% of the ocean. While the North Atlantic Ocean in Figure 4.6a shows a positive anomaly in the depths, a negative heat signal can be seen in the Pacific basin (Figures 4.5 and 4.6b). There, only a minimal fraction of the total heat is accumulated below 2000 m, under that threshold the Pacific loses heat. The processes in the model, which may lead to these signals in the vertical extent will be discussed in the following sections.

Figure 4.6 gives a first insight into regional heat distribution dependent on latitude. Most heat is stored in the subtropics as a result of its high heat uptake efficiency (Winton et al., 2010) whereas storage in the tropics is largely reduced as a result of high evaporation rates (Gill, 1982). The following three maps in Figure 4.7 show the total integrated heat anomaly (a) as well as the integrated anomalies over the upper ocean (b) and the deep ocean (c).
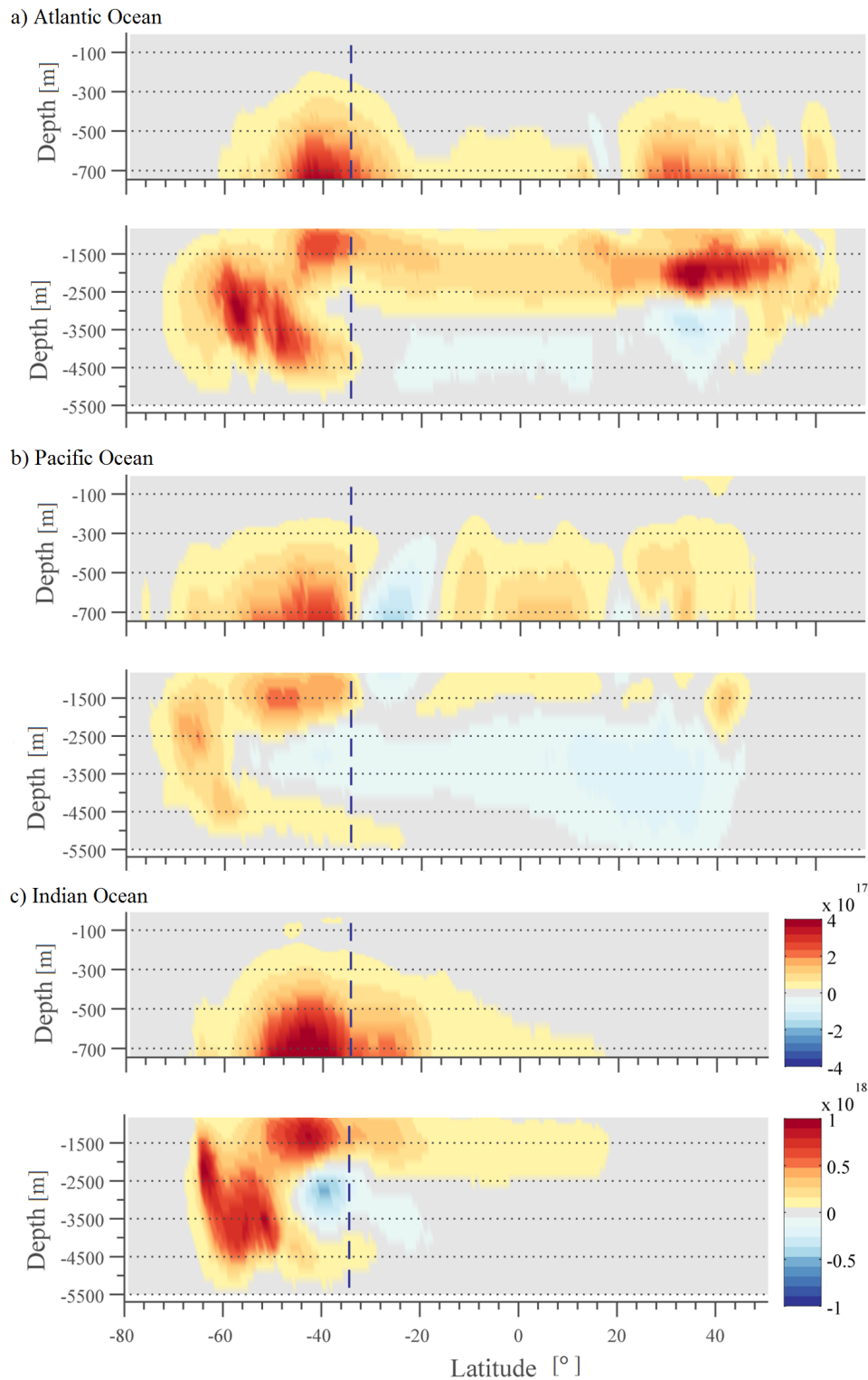
FIGURE 4.6: Zonally integrated heat content for the a) Atlantic, b) Pacific and c) Indian Oceans. The depth profiles are divided into the upper and deep oceans as defined in Figure 4.5. The colour bars and latitudinal scale shown in Subfigure c) also apply to the respective upper and deep ocean profiles in a) and b). The saturated colour scale is used to compare the three basins and includes values higher than indicated. The dashed vertical line at 34°S indicates the boundary between the individual ocean basin and the Southern Ocean at 34°S. The latitudinal axis in a) and b) include areas until 80°N while the one in c) ends at ∼ 60°N. The Southern Ocean boundaries between the three basins are defined in the same way as in 4.3.1, i.e. at 22°E, 145°E and 70°W.

a) total integrated heat anomaly
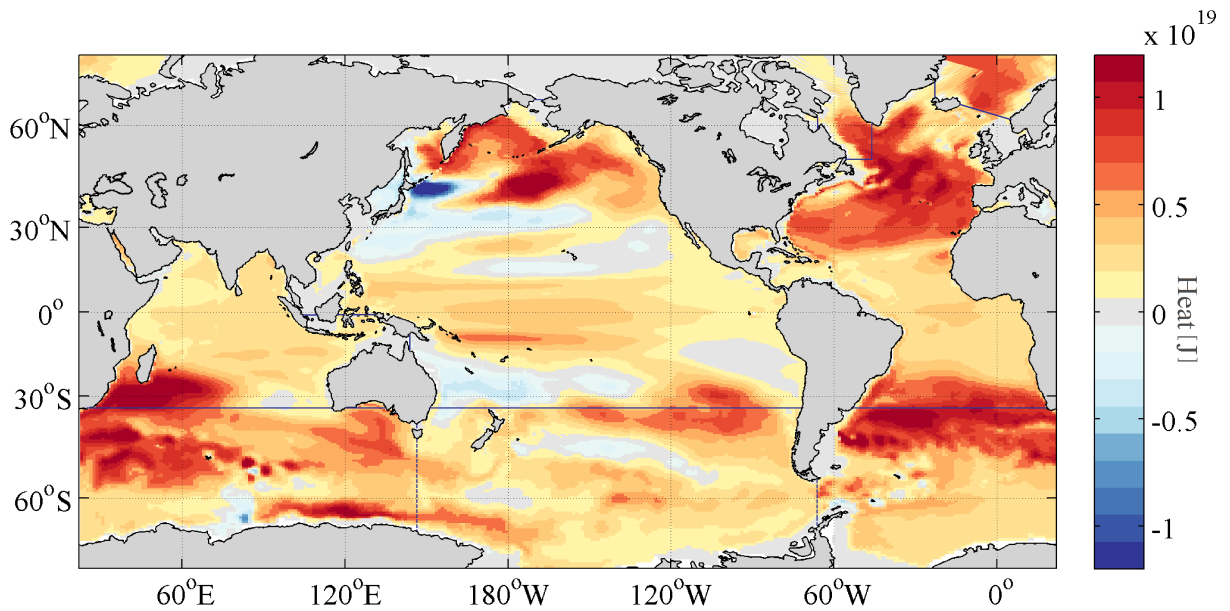
b) upper ocean   c) deep ocean
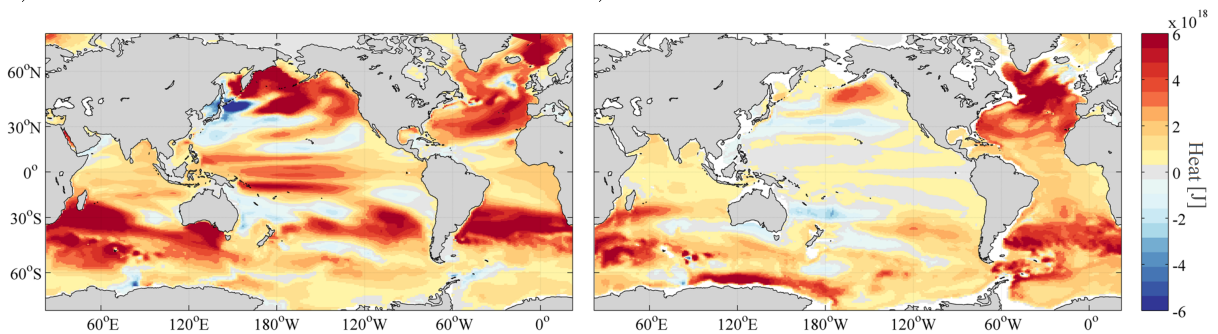
FIGURE 4.7: Integrated heat content over a) the entire water column, b) upper ocean and c) deep ocean. The dark blue solid separate the individual ocean basins in the model. The dashed lines between Antarctica and Australia / South America indicate the boundaries defined for Figure 4.6 and for the comparisons with observed data in Figure 4.4. The colour bar values in b) and c) are representing 50% of the interval in a).

As expected from the cross-sections in Figure 4.6, most heat in Figure 4.7 is stored south-wards of 30°S in the Southern Hemisphere as well as in the North Atlantic Ocean. The next three sections will describe in detail how ocean circulation plays a key role in heat uptake, distribution and storage.

4.3.3 Heat Anomaly in the Southern Ocean

Heat uptake in the modelled Southern Ocean takes place in areas of the ACC and near the Antarctic coast where upwelling occurs (see also Section 2.2.1 on Southern Ocean circulation). Similar to observations, the newly exposed water masses are cold, can absorb large quantities of heat from the atmosphere, and transport it northward (Morrison et al., 2015). This process may lead to the substantial heat storage around 30°S, especially in the upper 747 m (see Figure 4.7b). Unexpected is the decreased heat anomaly in the Pacific sector of this area. Whereas the Indian and Atlantic Southern Ocean sectors show heat storage of more than 6×10^{18}J, the area between $160°$E $- 60°$W in the Southern Ocean roughly stores ½ of the other sectors' heat. A delayed Southern Ocean warming in this area has also been observed in other CMIP5 models (Armour et al., 2016) during the time period $1982 - 2012$. The CMIP5 ensemble mean shows no temperature trend for $1982 - 2012$ north of the Ross Sea (Armour et al., 2016), which is slightly less than the temperature trend of this specific model (CCSM4 used here shows a mean trend of $0.002°$C/year; see also Figure 4.3). A reduced temperature trend in this region is also leads to a reduced heat storage rate. Less storage in the Ross Sea, especially further north, at 30°S, is according to Frölicher et al. (2015) most probably due to the model's internal variability. This paper states that averaged from $30°$ - $90°$S, internal variability accounts for 48% of the CMIP5 multi-model spread. It could be that reduced or even negative heat anomalies in the Pacific sector are connected to a local weakening in the ACC circulation or locally reduced atmospheric greenhouse gas forcing.

The deep ocean warming signal near the Antarctic coast in Figures 4.6c and 4.7c may be attributed to AABW formation. However, CMIP5 models in general encounter difficulties with creating dense water on the Antarctic shelf and especially in the deeper layers (Heuzé et al., 2013). Out of the 15 CMIP5 models investigated by Heuzé et al. (2013) (CCSM4 was not part of this analysis), only ten models create dense water in shelf areas. Instead, Heuzé et al. (2013) states that most models create deep water by open ocean convection which is a process that rarely occurs in reality. Therefore, this specific positive heat signal

in $1500 - 4500$ m depth cannot be fully explained. A further analysis similar to Heuzé et al. (2013) would be needed to arrive at more precise conclusions.

When recalling the temperature trend map in Figure 4.3, it is now possible to explain the high thermosteric trend in the Southern Ocean around 30° latitude. A high heat anomaly in the upper ocean's AAIW masses and a high temperature trend (see Figure 4.2b and a mean modelled initial temperature of $12 - 15$°C leads to this anomalous thermosteric sea level rise. This is in contrast to the area near the Antarctic coast between 100°-140°E. There, a large temperature trend in connection with a high heat anomaly did not lead to any sea level rise by thermal expansion. This can be explained by the low initial temperatures of -1° to 3°C and by the minor influence of a high temperature trend on small ocean volumes. As can be seen in Equation 3.4 ($V = V_0 \alpha \Delta T$) thermosteric sea level rise is also dependent on the initial volume. Thus, small ocean volumes as in these shallow shelf regions, despite experiencing large temperature increases, only lead to small thermal expansion rates.

4.3.4   Heat Anomaly in the North Atlantic Ocean

The Atlantic Ocean, while covering only 17% of the modelled ocean area, is responsible for 40% of the deep ocean heat storage below 747 m (see Table 4.2). This strong signal can both be seen in the cumulative ocean heat (Figure 4.5), in the cross-sectional Figure 4.6a and in the three maps presented in Figure 4.7. The Atlantic Ocean accumulates 20% less heat than the Pacific Ocean in the upper layers but due to its deep ocean circulation stores 12% more heat. In the Atlantic Ocean, 50% of the heat content change takes place in the upper and 50% in the deep ocean (Figure 4.6a and Table 4.2).

Especially of interest is the North Atlantic, where warm NAC water masses are transformed into cold and dense NADW (see also Section 2.2.2 on North Atlantic Ocean dynamics). The Atlantic Meridional Overturning Circulation (AMOC) plays an integral role in transporting the modelled heat from the surface into the lower ocean basin. Deep water formation, as mentioned in 2.2.2 occurs in the Labrador, Irminger and Greenland Seas. Figure 4.8 represents the cumulative vertical heat storage in three basins which include

these locations. The boundaries of the subbasins are shown in Figure 4.9a and include the Labrador Sea northwest of Newfoundland, Greenland, and the Hudson Bay, the Nordic Seas covering areas north of Iceland until 80°N and 22°E as well as the North Atlantic Ocean between 40°N and the boundaries of the other two basins. As above for the global distribution, Table 4.3 accompanies the figure by presenting the calculated values. Since cumulative heat content change at 3000 m depth is almost 100%, the abyssal depth would not have added any new insights. Besides, the modelled bathymetry, i.e. the underwater equivalent of topography, in this part of the Northern Atlantic very rarely reach such great depths.
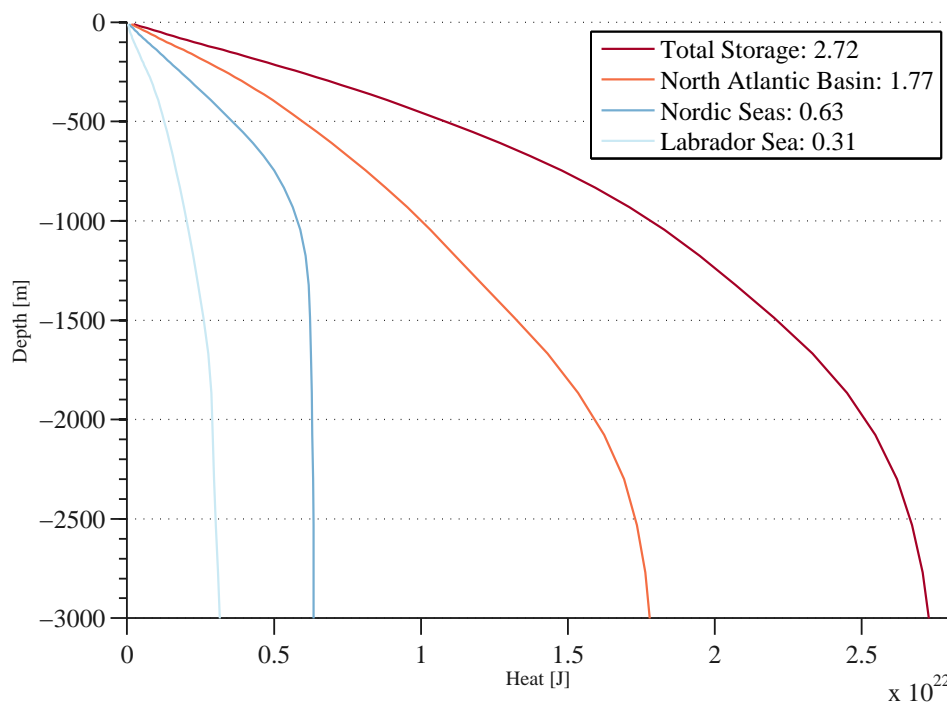
FIGURE 4.8: a) Modelled cumulative heat content change for the Labrador and Nordic Seas and the North Atlantic Ocean as defined by the solid lines in Figure 4.9a. The Labrador Sea in ice blue stores a total of 0.31×10^{22}J or 11.4% of the total heat content accumulated in this region. The Nordic Seas in darker blue with 0.63×10^{22}J (23.16%) and the North Atlantic area in orange with 1.77×10^{22}J (65.5%) have accumulated the remaining heat content. Values in the legend to the upper right indicate total heat uptake for this time period in 10^{22} Joule.

Depth Interval	Heat Content Change	Contribution
$0 - 500$ m	1.09×10^{22}	40.05%
$500 - 1000$ m	0.73×10^{22}	26.93%
$1000 - 1500$ m	0.37×10^{22}	13.63%
$1500 - 2000$ m	0.34×10^{22}	12.61%
$2000 - 2500$ m	0.12×10^{22}	4.58%
$2500 - 3000$ m	0.05×10^{22}	2.13%

TABLE 4.3: Heat content change in the North Atlantic limited by $40°N - 80°N$. In the second column are the calculated values as incremental depth intervals in Joule and in the third column as a percentage of the total.

The Labrador Sea stores, due to its small extent in both horizontal and vertical scale, the least amount of heat. Heat accumulation in the upper 500 m of the Nordic Seas basin is 60% the amount of the North Atlantic basin while covering only a fourth of its area. The Nordic Seas outflow is restricted to specific locations due to the Mid-Atlantic Ridge and the shallow modelled Faeroe $-$ Iceland Ridge and Denmark Strait (see also Figure 4.9). Heat storage within the Labrador Sea is less restricted by its shallow bathymetry and smaller due to its nearby located Subpolar Gyre, which positively impacts water mass transport southwards. While 51.8% of the total heat content in this region is stored in the upper ocean, a considerable amount reaches lower depths. This signal might arise as a result of warmer and less cold water masses sinking down into the lower depths similar to what is mentioned in Section 2.2.2. However, these water masses are still dense enough to get transported into the deep ocean. The average weighted North Atlantic deep ocean warming signal of $+0.04°$C in the depth layers 1000 m $-$ 2000 m may originate from the Labrador and Nordic Seas (and spread out as overflow water) into the deeper North Atlantic Ocean. It is also possible that NADW formation in the model is not restricted to those two locations and can also occur as a result of open ocean convection in the North Atlantic. A more detailed analysis of the origin of these less cold water masses would be needed to confirm this assumption.
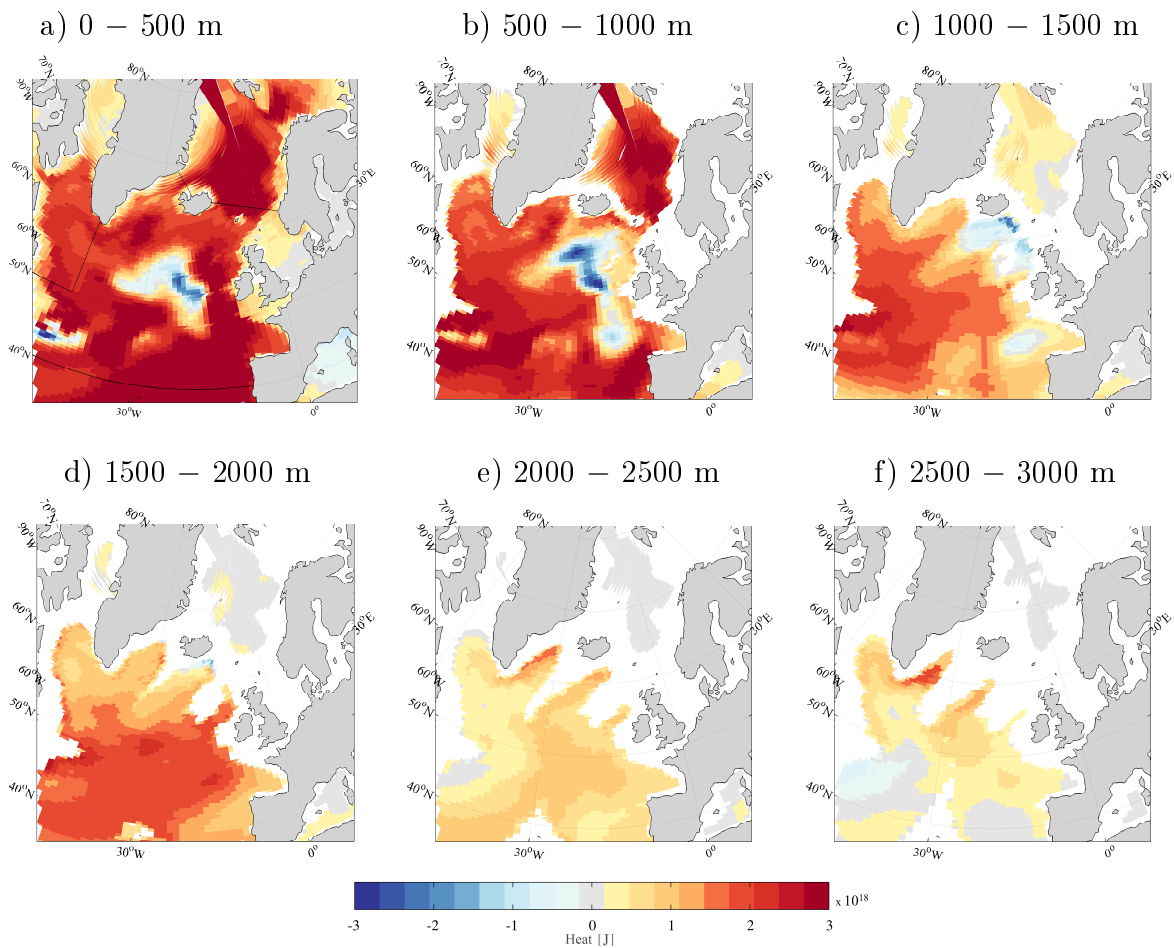
FIGURE 4.9: Integrated North Atlantic heat content change between 40°N − 80°N in various depths intervals. The solid black lines in a) represent the boundaries between Labrador Sea, Nordic Seas and the North Atlantic used for Figure 4.8 and Table 4.3. Each panel represents the heat content in subsequent 500 m depth intervals. White colouring is indicating where there are no values, i.e. where the ocean bottom is reached. Black lines in the 0 − 500 m projection represent boundaries between the Labrador Sea, the Nordic Seas and the North Atlantic Ocean as defined for Figure 4.9 and Table 4.3. The area with constant values at 0° longitude in northwestern Greenland appeared due to a regridding error during the mapping process and and does not have a negative influence.

Additionally, the 0 − 500 m integrated heat anomaly in the North Atlantic is negatively influenced by the loss in the central North Atlantic Ocean. This signal in Figure 4.9a propagates northeastwards with depth until it reaches the ocean floor at 1500 m. This negative heat anomaly, which is also visible in the temperature trend (Figure 4.3) may be linked to a reduction in the AMOC (Rahmstorf et al., 2015). A weakening of the AMOC could be caused by reduced NAC density. Observations of sea surface temperture since 1901 linked a weaker circulation with increased melting of the Greenland Ice Sheet

and associated freshwater input (Rahmstorf et al., 2015). However, a dynamic Greenland Ice Sheet and its variability in freshwater forcing are not simulated in this version of the CCSM4 model (Lenaerts et al., 2015). It may be that the cause of this anomaly is a different one. This specific temperature/heat anomaly signal is also appareant in the CMIP5 ensemble mean where it generally shows a much weaker subpolar cooling than the observations (Drijfhout et al., 2012). The main difference between the simulated and observed 'warming hole' is suspected to be that the models' AMOC stability is overestimated in regards to freshwater input (Hofmann and Rahmstorf, 2009) or that most models miss an important forcing in Greenland meltwater runoff (Rahmstorf et al., 2015).

Coming back to the temperature trend (Figure 4.3) and thermosteric sea level rise (Figure 4.2), the different trends in the North Atlantic can now be explained with regards to the ocean warming. The North Atlantic area including the Greenland and Labrador Seas display some of the highest temperature trends. Initial temperatures are in the range of $0-4°C$ in the Greenland, Labrador and Irminger Seas whereas higher initial temperatures of $10°C$ south of Iceland and even up to $16°C$ can be found in the southernmost parts of this sector (see Figure 4.10). The high initial temperature southeast of the Irminger Sea is a result of the NAC. The high heat anomaly in intermediate depths is caused by high surface absorption or less heat loss in surface waters around Greenland and subsequent vertical transport into the ocean's interior. The heat anomaly in 2000 m depth (Figure 1.2a) is caused by warmer water masses than the anomaly in the Southern Ocean since it also causes a larger thermal expansion trend (see Figure 4.2). The highest thermal expansion trends in the North Atlantic are concentrated in the Irminger Sea. There, water masses warmed the most whereas the remaining heat signal is accumulated in colder water masses. Additionally, outflowing warm and saline water masses from the Mediterranean Sea may also play a role in this regions heat anomaly/thermal expansion trend since high thermal expansion trends are also simulated near the eastern border of the Atlantic Ocean at $30°N$.
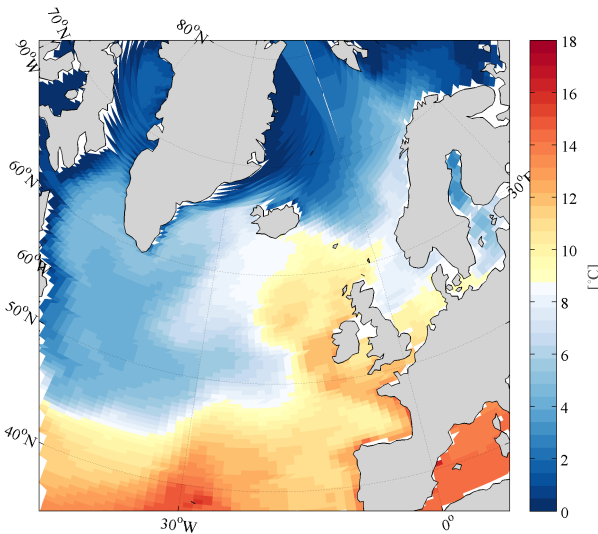
FIGURE 4.10: a) Initial temperature distribution in the North Atlantic Ocean for the upper ocean including 0 − 747 m depth.

4.3.5 Heat Anomaly in the Pacific Ocean

Most of the heat storage in the Pacific is either restricted to the North Pacific between 40°N − 60°N or the central western Pacific. The heat anomaly around 30°S is most likely governed by the Southern Ocean dynamics discussed above. In the high latitude North Pacific the positive heat anomaly is limited to the upper ocean and does not reach lower depths (see Figure 4.7b. Contrary to the Southern and the North Atlantic Oceans, there is no deep water formation in the Pacific. As can be seen in the cumulative heat content (Figure 4.5), 88% of the Pacific heat anomaly is located in the upper 400 m. An intensification of the Kuroshio Current off the coast of Japan may bring more heat into the higher latitudes of the Pacific Ocean (Seager et al., 2001). It is currently unclear why there is a strong modelled negative heat anomaly east of Hokkaido, the northernmost of Japan's main islands where the Kuroshio Current naturally flows through. Due to time constraints, it is not possible to look into detail how the this current is modelled within the CCSM4 and how it may affect the heat anomaly in the North Pacific Gyre.

A weakening of the cyclonic turning North Pacific Gyre circulation may also have played a role in this region's heat storage. Due to the Coriolis Force, water masses inside this gyre are deflected to the right, converge and lead to downwelling (Bearman et al., 1989). Less downwelling inside the gyre would mean that water masses close to the surface accumulate more heat and would explain the positive heat anomaly.

The upper ocean heat anomaly in the western equatorial Pacific, as mentioned in Section 4.2, may be linked to the models' assymetry of ENSO phases. A modelled trend in stronger La Niña events throughout the full time period can lead to this positive signal. The two areas of the Pacific Ocean explained here have different effects on thermosteric sea level rise. The assumed North Pacific Gyre heat anomaly has minimal impact on thermal expansion because cold initial temperatures of $\sim 5°C$ in connection with a weaker temperature trend than the Atlantic Ocean at same latitudinal angle prevent it. The ENSO asymmetry is likely responsible for the modelled mean annual thermal expansion trend of 6 mm/year as a result of high equatorial initial temperatures between $20° - 23°C$ and a significant temperature trend.

4.3.6   3D Temperature - Salinity Diagrams

The last three sections showed that most heat is accumulated in the Subtropics, either in the Southern or the North Atlantic Ocean. Figure 4.11a shows the total heat content anomaly in dependence temperature and salinity. Most of the heat is accumulated in water masses with high salinity $(33 - 35 gkg^{-1})$ and colder temperatures in the range of $6° - 21°C$). Water masses which lost heat or show a negative thermal expansion trend are hard to see due to concealment of other bars. As introduced in Section 2.1, the highest thermal expansion trends occur in water masses with high temperatures and can be seen in Figure 4.11b). Concluding from the two diagrams, it is clear that at constant salinity of $32g/kg$, heat storage is larger in cold than warmer water masses yet thermal expansion trends show a higher amplitude in warmer than in colder waters.

a) heat content
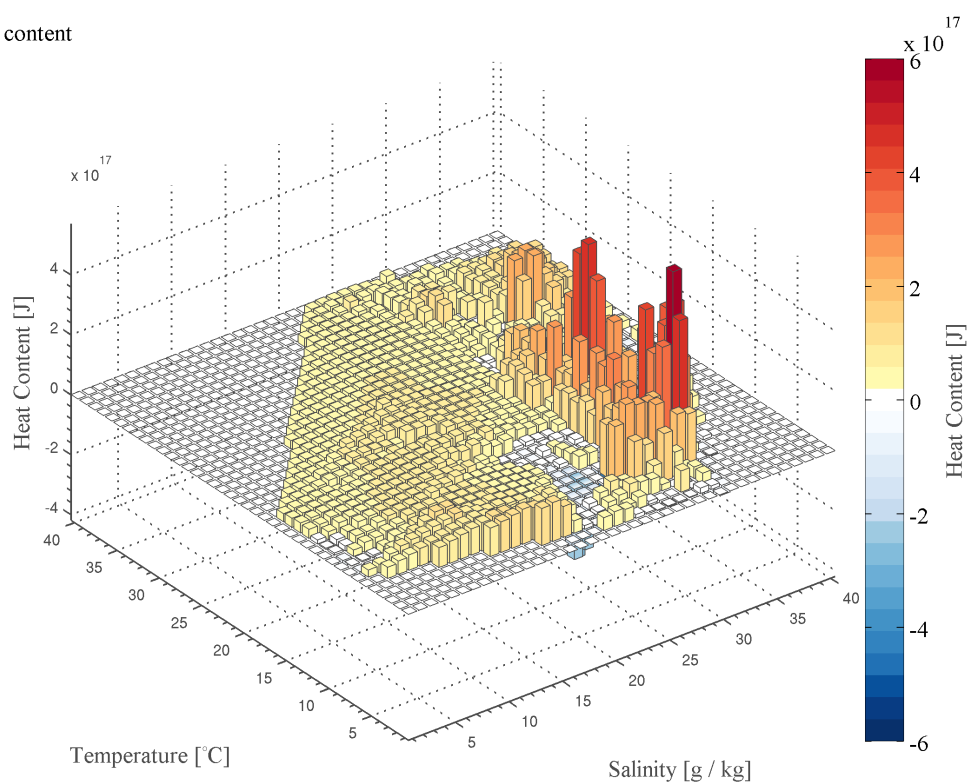
b) thermal expansion
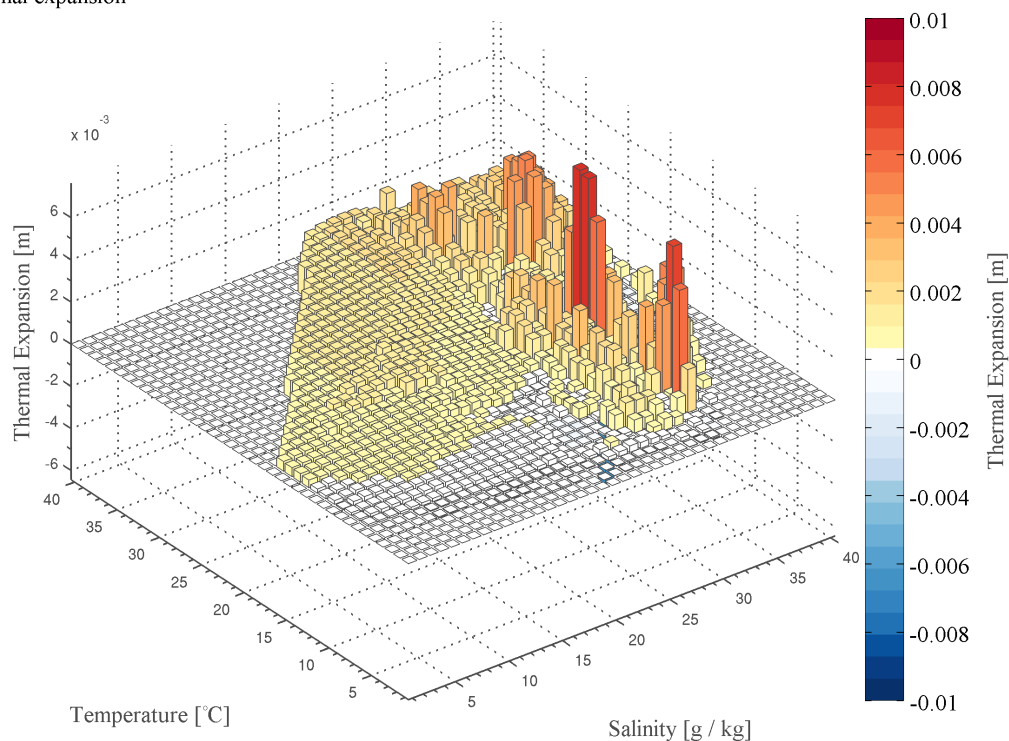
FIGURE 4.11: Three-dimensional temperature-salinity diagrams. In a) the height and colour of the individual bars show how much heat is accumulated in a specific water mass with a certain salinity and conservative temperature and in b) how much those water masses expanded over the 24-year period. A white area indicates water masses that do not appear in the model or water masses which did not accumulate heat or expanded. A resolution of 0.1°C and 0.1 g/kg was used so water masses with a temperature of 5.17°C contribute their values to the 6°C bar.

Chapter 5:   Conclusions and Outlook

5.1   Summary and Conclusions

Atmosphere - Ocean General Circulation Models are an integral part of understanding the climate system of the past, present and the future through projections. On the basis of sea level rise through thermal expansion it was calculated where and why increasing temperatures in the ocean affect its volume. By applying a linear trend to the conservative temperature values in each model grid cell, natural variability was smoothed out. Additionally, subtracting the long - term model drift further helped isolating the anthropogenic signal.

Comparisons with observed and modelled data sets on the global scale verified the calculated thermal expansion trend of 1.5 mm/year, the global heat anomaly of 2.24×10^{23} Joules and the individual basin trends.

The non - linear relation between temperature increase and density of seawater showed that the rate of thermal expansion is strongly dependent on initial conditions. Warming cold and warm water masses by the same amount leads to different rates of density / volume decrease and to various thermoseric sea level rise. The total integrated temperature change during the last 24 years showed four regions with high trends, those being the Southern Ocean around 30°S, the coastal areas near the Antarctic coast, the North Atlantic Ocean and the western equatorial Pacific Ocean. As expected, the Western Pacific Warm Pool with high initial temperatures also exhibits the highest thermal expansion trend. The considerable thermal expansion in the North Atlantic arises due to a different mechanic.

As warm and saline water masses in the North Atlantic Ocean move northwards, they cool and sink as a result of their increased density. One of the globally highest temperature trends leads to heat uptake before the water masses sink down into depths of 2500 m. The increased temperature does not yet have that large of an impact that sinking is fully prevented. This positive heat signal in the deep ocean eventually leads to thermal expansion of the water column. While high heat storage in the North Atlantic is responsible for the

high thermosteric trend, the opposite is true for the Southern Ocean. Upwelling of deep water masses, high surface absorption and equatorward transport by the Coriolis force stores most heat in the upper ocean when these water masses subduct under the warmer tropical waters. The thermal expansion trend in this latitudinal band around 30°S, where large amounts of heat are stored in the ocean, does not deviate from the surrounding trends as a result of cold temperatures of these waters.

An analysis of the properties of global water masses showed that cold and high saline conditions are beneficial for long-term storage within the ocean interior. The high heat storage areas in the Southern Ocean and the North Atlantic both represent similar low temperature and high salinity conditions.

In conclusion, it can be said that the model's simulation of heat uptake and storage is successful for expected regions. The model encountered difficulties with simulating the Kuroshio Current at the western border of the Pacific Ocean.

5.2   Possible Improvements and Future Work

As briefly mentioned above, a multi-model mean of several CMIP5 models would have resulted in more precise results as the CCSM4's internal variability would have been smoothed out. As stated in Frölicher et al. (2015), internal variability, especially in the Southern Ocean south of 30°S accounts for 48% of the CMIP5 ensemble mean spread.

By using a linear trend approximation during the 24-year time period it was assumed that thermal expansion is linear. A year-by-year calculation would have resulted in more precise data where regional variability is clearer shown.

Further investigation into the model's ocean circulation and its mechanics especially in regards to deepwater formation near shelf areas and heat loss in the deep Pacific Ocean would prove useful in more clearly determining the origin of the waters' heat signals.

Thermal expansion patterns in the eastern Atlantic Ocean are influenced by Mediterranean Overflow Water (Talley, 2000), an analysis of this high saline water mass would give more insights.

Greenland freshwater forcing was not implemented in this version of CCSM4, a clearer insight into the North Atlantic Warming Hole would have resulted with calculations from the most recent model output.

The impact of internal oscillations such as the Pacific Interdecadal Oscillation and the Atlantic Meridional Oscillation with periods of 10 (England et al., 2014) respectively 65 - 70 years (Schlesinger et al., 1994) on heat storage during the investigated time period has not been mentioned although they influence heat uptake. A closer investigation would be insightful.

The analysis for the last 24 years has been done to check the correctness of the model's own climate system for it to be used to project the future's changes in how the atmosphere and ocean circulation governs ocean warming. Figure 5.1a shows how ocean temperature values may increase until the end of the century in dependence of two representative concentration pathways defined in the IPCC reports (Van Vuuren et al., 2011). The map in 5.1b represents the calculated heat anomaly with rcp85 data until the end of the century. No model drift correction has been done yet.

a)   b)

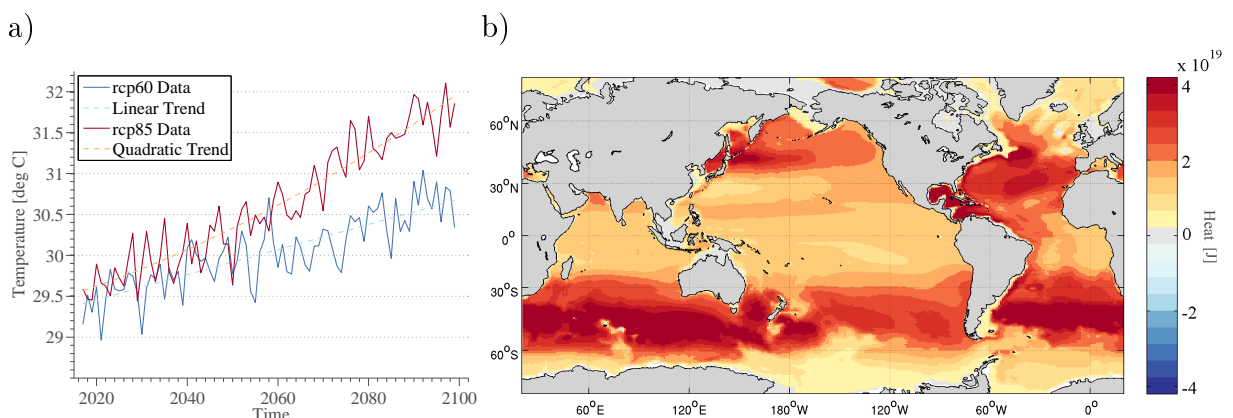FIGURE 5.1: a) Future temperature trend in grid cell [1,140,190] near Fiji in dependence of two future gas emission scenarios. For future projections, different scenarios are used. Shown here are Representative Concentration Pathways rcp60 and rcp85 (i.e. a global warming potential of +1.3°C / +2.0°C until 2100). b) Modelled total integrated heat content anomaly 2017 - 2100 in dependence of rcp85.

Appendix A: Matlab Scripts

```matlab
 1  % --- Script for Calculations --- %
 2
 3  % Calculate conservative temperature trend, thermal expansion contribution
 4  % to sea level rise and ocean heat content with the CCSM4 AOGCM for the
 5  % time period 1993 - 2016
 6
 7  filename1 ='/net/atmos/data/cmip5/historical/fx/volcello/CCSM4/r0i0p0/';
 8  filename2 ='/net/atmos/data/cmip5/historical/fx/areacello/CCSM4/r0i0p0/';
 9  filename3 ='/net/atmos/data/cmip5/historical/Omon/so/CCSM4/r1i1p1/';
10  filename4 ='/net/atmos/data/cmip5/historical/Omon/thetao/CCSM4/r1i1p1/';
11  filename5 ='/net/atmos/data/cmip5/rcp85/Omon/thetao/CCSM4/r1i1p1/';
12  filename6 ='/net/atmos/data/cmip5/historical/fx/deptho/CCSM4/r0i0p0/';
13  filename7 ='/net/atmos/data/cmip5/historical/Omon/zos/CCSM4/r1i1p1/';
14  filename8 ='/net/atmos/data/cmip5/rcp85/Omon/zos/CCSM4/r1i1p1/';
15
16
17  %% load in grid cell volume (volcello), area (areacello), total depth (deptho),
18  %% depth of each grid cell (lev_bnds), latitude (lat) and longitude (lon)
19
20  volcello = getnc([filename1 'volcello_fx_CCSM4_historical_r0i0p0.nc'], 'volcello');
21  areacello = getnc([filename2 'areacello_fx_CCSM4_historical_r0i0p0.nc'], 'areacello');
22  deptho = getnc([filename6 'deptho_fx_CCSM4_historical_r0i0p0.nc'], 'deptho');
23  lev_bnds = getnc([filename4 'thetao_Omon_CCSM4_historical_r1i1p1_196001-196912.nc'], ...
24      'lev_bnds');
25  lev_bnds(:,3) = lev_bnds(:,2) - lev_bnds(:,1);    % 3rd row: height of each layer
26
27  % lat and lon are [384,320] arrays
28  lat=getnc('/net/atmos/data/cmip5/historical/Omon/zos/CCSM4/r1i1p1/
        zos_Omon_CCSM4_historical_r1i1p1_185001-200512.nc','lat');
29  lon=getnc('/net/atmos/data/cmip5/historical/Omon/zos/CCSM4/r1i1p1/
        zos_Omon_CCSM4_historical_r1i1p1_185001-200512.nc','lon');
30
31
32  %% store variables in specified empty arrays which get filled up each iteration
33
34  % ocean grid is defined as [60,384,320] -> [depth,long,lat]
35  % nan = not-a-number -> empty cell
36  so = nan(60,384,320);                  % initial absolute salinity in year 1993
37  ct = nan(60,384,320);                  % initial conservative temperature in year 1993
38  p = 0;                                 % pressure at sea surface -> 0dbar
39
40  delta_ct = nan(60,384,320);            % trended conservative temperature difference
41  alpha = nan(60,384,320);               % thermal expansion coefficient
42  delta_temperature = nan(60,384,320);   % depth scaled cons. temperature trend
43  delta_volume = nan(60,384,320);        % volume difference due to thermal expansion
```

```matlab
44  delta_height = nan(60,384,320);        % sea level rise due to thermal expansion
45
46  cp = gsw_cp0;                          % specific heat capacity 3.99e+03 J / (kg * K)
47  rhopoto_in = nan(60,384,320);          % initial potential density 1993
48  rhopoto_fin = nan(60,384,320);         % final potential density 2016
49  delta_heat_in = nan(60,384,320);       % initial heat content 1993
50  delta_heat_fin = nan(60,384,320);      % final heat content 1993
51  heat_diff = nan(60,384,320);           % heat difference
52
53
54  %% load in initial salinity and conservative temperatures in year 1993
55  get1 = getnc([filename3 'so_Omon_CCSM4_historical_r1i1p1_199001-199912.nc'], ...
56      'so', [37,1,1,1],[48,-1,-1,-1],[1,1,1,1]);  % load in 12 months of data
57  so = squeeze(nanmean(get1)); clear get1;       % calculate annual mean salinity
58  so = so.*1000;                                 % convert into [g / kg]
59
60  get1 = getnc([filename4 'thetao_Omon_CCSM4_historical_r1i1p1_199001-199912.nc'], ...
61      'thetao', [37,1,1,1],[48,-1,-1,-1],[1,1,1,1]);
62  thetao = squeeze(nanmean(get1)); clear get1;
63
64  % convert potential temperature into conservative temperature array
65  for z = 1:60;                  % loop through all depth levels
66      for x = 1:384;             % loop through full longitude
67          for y = 1:320;         % loop through full longitude
68              % use potential temperture in [degree C] so GSW function can
69              % work with it
70              ct(z,x,y) = gsw_CT_from_pt(so(z,x,y),thetao(z,x,y)-273.15);
71          end
72      end
73  end
74  % convert conservative temperature output back to [K]
75  ct = ct + 273.15; clear thetao z x y;
76
77
78  %% load in monthly potential temperature data, calculate the annual mean for each of the
79  %% 24 years, convert values into conservative temperature, fit 1-st order polynomial
80  %% function, calculate alpha , calculate conservative temperature difference and
81  %% volume change because of it
82
83  Nt=24; % number of years
84  year_list = 1993:2016; % array with year values
85
86  % load in monthly potential temperature values
87  for z = 1:60;     % loop through all depth levels
88  tic               % measure how long it takes to get data (~ 60 seconds per level)
89      get1 = getnc([filename4 'thetao_Omon_CCSM4_historical_r1i1p1_199001-199912.nc'], ...
90      'thetao', [37,z,1,1],[-1,z,-1,-1],[1,1,1,1]);
91      get = get1; clear get1;
```

```matlab
92       get1 = getnc([filename4 'thetao_Omon_CCSM4_historical_r1i1p1_200001-200512.nc'], ...
93       'thetao', [1,z,-1,-1],[-1,z,-1,-1],[1,1,1,1]);
94       get(85:156,:,:,:) = get1; clear get1;
95       % Since historical model data is only available until the end of 2005,
96       % rcp85 data is used for the remaining years
97       get1 = getnc([filename5 'thetao_Omon_CCSM4_rcp85_r1i1p1_200601-200912.nc'], ...
98           'thetao', [1,z,-1,-1],[-1,z,-1,-1],[1,1,1,1]);
99       get(157:204,:,:,:) = get1; clear get1;
100      get1 = getnc([filename5 'thetao_Omon_CCSM4_rcp85_r1i1p1_201001-201912.nc'], ...
101          'thetao', [1,z,-1,-1],[84,z,-1,-1],[1,1,1,1]);
102      get(205:288,:,:,:) = get1; clear get1;
103
104      % get(288,60,384,320) now contains monthly thetao data for the 24 years
105      % in every grid cell -> that's a lot of values: 2.12e+09 different values
106      % however, I only load in one depth level at a time; do everything and
107      % then go one level deeper
108  toc
109  tic               % measure how long calculations take (~120 seconds)
110      for x = 1:384;  % loop through full longitude
111
112              for y = 1:320; % loop through full longitude
113
114              %% convert potential temperature into conservative temperature
115              % for CT and alpha calculation, temperature in [deg C] is needed
116              % reshaping my potential temperature array to get 24 rows
117              % each containing the monthly values and then calculate the
118              % mean of every row
119
120              get_ann=reshape(get(:,x,y),12,24); % get_ann = [12x24]
121              get_ann_mean = nanmean(get_ann); % get_ann_mean = [1x25]
122
123              % convert annual mean potential temperatures to
124              % conservative ones
125
126              % ----------------------------------------------------------------------%
127              %                                                                        %
128              % potential temperature -> conservative temperature with gsw_CT_from_pt %
129              %                                                                        %
130              % ----------------------------------------------------------------------%
131
132              for u = 1:24;
133                  get_ann_mean(u) = gsw_CT_from_pt(so(z,x,y),(get_ann_mean(u)-273.15));
134              end
135
136              % fitting first-order polynomial function, aka linear trend
137              % polyfit(x,y,n); x-axis, y-axis, n = 1 (order of polynomial fit)
138              fit=polyfit(1:Nt,get_ann_mean,1);
139
```

```
140                % ts = define linear function from the fit: y = a*x + b
141                % ts = [1,24] array with steady linear temperature change
142                ts=fit(1)*(1:Nt)+fit(2);
143                clear fit;
144
145                %% calculate thermal expansion coefficient alpha
146
147                % ------------------------------%
148                %                               %
149                % alpha -> gsw_alpha_CT_exact   %
150                %                               %
151                % ------------------------------%
152
153                alpha(z,x,y) = gsw_alpha_CT_exact(squeeze(so(z,x,y)),ts(1),p);
154
155                %% save total difference of temperature trend in array
156                delta_ct(z,x,y) = (ts(24)-ts(1));
157
158                %% calculate change volume due to thermal expansion
159
160                % ---------------------------------------------------------%
161                %                                                          %
162                %       volume change = V(0) * alpha * (T(25) - T(1))       %
163                %                                                          %
164                % ---------------------------------------------------------%
165
166                delta_volume(z,x,y) = volcello(z,x,y)*alpha(z,x,y)*delta_ct(z,x,y);
167
168            end              % end of longitude loop
169        end                  % end of latitude loop
170 toc
171 end                        % end of depth loop
172
173
174 %% calculate sea level rise due to temperature change
175 for z = 1:60;              % loop through full depth levels
176     for x = 1:384;
177         for y = 1:320;
178
179                % ------------------------------%
180                %                               %
181                %     height = volume / area     %
182                %                               %
183                % ------------------------------%
184
185                delta_height(z,x,y) = (delta_volume(z,x,y) ./ areacello(x,y));
186         end
187     end
```

```matlab
188  end
189
190  % for plotting routines, since we can only have a 2d map, sum up the total height
191  % change in the depth dimension
192  height = squeeze(nansum(delta_height)./24); % divide by 24 to get thermal expansion
193                                              % trend per year
194  height(height == 0)=nan;                    % set zero values to nan so land areas
195                                              % are white in the map
196
197  % for the plotting routines, the longitudinal, latitudinal and data arrays
198  % got rearranged so the Pacific was in the middle and an empty grid cell
199  % line at zero latitudes, where two maps were overlaid, was avoided
200  [newlon newlat newheight] = rearrange_CCSM4(lon, lat, height);
201
202
203  %% weighted temperature trend and its average over full column
204  % scale the temperature in each grid cell by the level, since it is a relative value
205  for z = 1:60;
206      for x = 1:384;
207          for y = 1:320;
208              delta_temperature(z,x,y) = delta_ct(z,x,y) * lev_bnds(z,3) ./ deptho(x,y);
209                                          % delta_Ti      * delta_Hi      ./   H
210          end
211      end
212  end
213
214
215  %% calculate heat content anomaly due to the temperature trend
216  % how much has ocean warmed in each grid cell?
217
218  % potential density change in every grid cell
219  % equation from http://teos-10.org
220  for z = 1:60;
221      tic
222      for x = 1:384;
223          for y = 1:320;
224              rhopoto_in(z,x,y) = gsw_rho(squeeze(so(z,x,y)),ct(z,x,y),p);
225
226              rhopoto_fin(z,x,y) = gsw_rho(squeeze(so(z,x,y)),ct(z,x,y)+delta_ct(z,x,y),p)
     ;
227          end
228      end
229      toc
230  end
231
232  % equation from Dijkstra, Henk A. (2008). Dynamical oceanography
233  % ------------------------------------------------------------%
234  %                                                             %
```

```matlab
235   % Heat(1) = rho(1) * cp * volcello * ct(1)                  %
236   % Heat(25) = rho(25) * cp * volcello * ct(1) + delta_ct        %
237   %                                                          %
238   % ------------------------------------------------------------%
239
240   for z = 1:60;
241       for x = 1:384;
242           for y = 1:320;
243               delta_heat_in(z,x,y) = rhopoto_fin(z,x,y) * cp * volcello(z,x,y) * ...
244                   (ct(z,x,y));
245               delta_heat_fin(z,x,y) = rhopoto_in(z,x,y) * cp * volcello(z,x,y) * ...
246                   (ct(z,x,y)+delta_ct(z,x,y));
247           end
248       end
249   end
250
251   % full ocean depth heat distribution
252   heat_diff = delta_heat_fin - delta_heat_in;
253
254   % difference in heat content between 1992 and 2016
255   % for upper ocean, I just take the first 37 depth levels: ... nansum(heat_diff(1:37)
256   heat = squeeze(nansum(heat_diff));  % averaged heat change over full ocean depth
257   heat(heat == 0)=nan;    % set cells with zero value as land
258   [newlon newlat newheat] = rearrange_CCSM4(lon, lat, heat);
259
260
261   %% the control run used the same structure with different files
262   load('workspace_piControl', 'delta_temperature_piControl', ...
263       'delta_height_piControl', 'heat_diff_piControl');
264
265   % subtracting the piControl values from the three output arrays
266   delta_temperature = delta_temperature - delta_temperature_piControl;
267   delta_height = delta_height - delta_height_piControl;
268   heat_diff = heat_diff - heat_diff_piControl;
269
270
271   %% saving workspace so nothing gets lost
272
273   filename9 = 'workspace_thermal_expansion_CCSM4_with_CT_rev5';
274   save(filename9)
```

```matlab
1   % --- Script for mapping --- %
2
3   %% load in necessary arrays from the earlier calculations
4   load('workspace_thermal_expansion_CCSM4_with_CT_rev5', 'newlon', 'newlat', ...
5       'RdYlBu','newheat');
6
7   % using the cbrewer package for the colour shading, a diverging scale from
8   % red -> yellow -> blue with 19 different colours
9   RdYlBu = cbrewer('div', 'RdYlBu', 19); % the one loaded in is slightly modified
10
11
12  figure(1);
13  colormap(flipud(RdYlBu)); % define the colour shading (blue -> yellow -> red)
14
15  % using the miller projection from the m_map package for lat / lon intervals
16  m_proj('miller','lat',[-75 75], 'lon',[22 382]);
17
18  % or using the azimuthal equal-area projection centered around 60 degrees North
19  % and 341 degrees East with a radius of 31 degrees and by using a rectangular box
20  m_proj('azimuthal equal-area','lat',60,'long',341,'radius',31, 'rectbox', 'on');
21
22  % colour in the values
23  h=m_pcolor(newlon, newlat, newheat); set(h,'linestyle','none'); hold on;
24  h=m_pcolor(newlon+360, newlat, newheat);set(h,'linestyle','none'); hold on;
25
26  % set the minimum and maximum values of the colour bar
27  set(gca, 'clim', [-1.2e+19 1.2e19]); hold on;
28  set( gca, 'FontName', 'Times New Roman', 'Fontsize', 12);
29
30  % activate the lon / lat grid, colour the coast lines black and the land grey
31  m_grid; m_coast('color',[.1 .1 .1]); m_coast('patch',[0.83 0.83 0.83]);
32
33  % plotting lines within the projection which get adjusted automatically
34  % here for example separating the Labrador Sea from the North Atlantic
35  m_line([304, 314],[51, 51], 'color', RdYlBu(19,:)); % m_line([lat],[lon])
36  m_line([314, 314],[51, 61], 'color', RdYlBu(19,:));
37
38  % set colour bar and define its unit
39  h=colorbar; h1=ylabel(h,'Joule', 'color', [.3 .3 .3]);
40  set( gca, 'FontName', 'Times New Roman', 'Fontsize', 12);
41
42  % save figure as eps vector graphic with resolution of 300dpi
43  print('-depsc','-r300', '/home/hmaurice/Plots/modelled_heat_content_change_1992_2016');
```

```matlab
1   % --- Script for plotting basin-wide cumulative heat --- %
2
3   load('workspace_thermal_expansion_CCSM4_with_CT_rev5', 'lev_bnds', '
        vertical_heat_global_ocean', 'vertical_heat_pacific', 'vertical_heat_southern', ...
4       'vertical_heat_atlantic', 'vertical_heat_indian', 'vertical_heat_mediterranean', '
        vertical_heat_nordic', ...
5       'vertical_heat_hudson', 'vertical_heat_greenland', 'vertical_heat_labrador', '
        vertical_heat_baltic', ...
6       'vertical_heat_indian2', 'vertical_heat_shelf', 'RdYlBu');
7
8   RdYlGn = cbrewer('div', 'RdYlGn', 19);
9
10
11  %% first, derive heat values for individual ocean basins
12  % the same routine is used for the other basins
13
14  %% global ocean vertical heat distribution
15  full_area = squeeze(nansum(squeeze(nansum(areacello)))); % 3.611e+14 square meters
16
17  for z = 1:60;   % loop through every depth level
18      s = find(isnan(squeeze(heat_diff(z,:,:)))== 0);
19
20      % sum up every depth level that does not contain zero values
21      vertical_heat_global_ocean(z) = sum(squeeze(heat_diff(z,s)));
22  end
23
24
25  %% pacific ocean vertical heat distribution
26  % load in grid mask, every grid cell that resembles Pacific has a 2 value in it
27  % change Pacific values to 1 and the rest to 0
28  pacific = getnc('ocean_grid_cesm104.f19_g16.340', 'REGION_MASK');
29  pacific(pacific ~= 2) = 0;
30  pacific(pacific == 2) = 1;
31  pacific(pacific == 0) = nan;
32
33  a = find(isnan(squeeze(pacific))== 0);
34  pacific_area = nansum(areacello(a)); % Pacific area without the zero value cells
35
36  test = nan(60,384,320);
37  for z = 1:60;
38      % multiply heat array * Pacific area , the other areas are all zero
39      test(z,:,:) = squeeze(heat_diff(z,:,:)) .* pacific;
40
41      % sum up the total heat in the Pacific for each level
42      s = find(isnan(squeeze(test(z,:,:)))== 0);
43      vertical_heat_pacific(z) = sum(squeeze(heat_diff(z,s)));
44
45  end
```

```matlab
46
47  % plotting routine starts here
48  figure(1);
49  % plot flipped upside-down array of cumulative ocean heat vs. - depth levels
50  % transpose to get the correct array dimension for plotting
51  plot(flipud(cumsum(vertical_heat_global_ocean')), -flipud(lev_bnds(:,2)), ...
52      'color', RdYlBu(1,:), 'LineWidth', 1.2); hold on;
53  plot(flipud(cumsum(vertical_heat_pacific')), -flipud(lev_bnds(:,2)), ...
54      'color', RdYlBu(1,:), 'LineWidth', 1.2); hold on;
55  % etc. for all other basins
56
57  h = legend('location', 'Best', 'World Ocean: 2.24', 'Southern Ocean: 0.43');
58
59  yPos1 = -203.6859; % set positions for labeling of upper and deep ocean within
60  yPos2 = -747.2829;
61  hold on;
62
63  hline = refline([0 -747.2829]); % draw boundary line between upper and deep ocean
64                                  % at -747 m depth
65  set(hline, 'LineStyle', '--', 'color', RdYlBu(15,:), 'linewidth', 1.2);
66
67  str = {'Upper Ocean'};
68  text(.9e+23,-600,str, 'FontName', 'Times New Roman', 'color', [.3 .3 .3])
69  hold on;
70  str = {'Deep Ocean'};
71  text(.9e+23,-2500,str, 'FontName', 'Times New Roman', 'color', [.3 .3 .3])
72
73  % label axes
74  xlabel('Heat (J)', 'FontName', 'Times New Roman', 'fontsize', 12); hold on;
75  ylabel('Depth (m)', 'FontName', 'Times New Roman', 'fontsize', 12); hold on;
76
77
78  axis([-.05e23,2.5e23, -6000 0])          % change axis limit for more fancy plot
79  set(gca, ...
80    'Box'         , 'off'     , ...        % no box drawn around plot
81    'TickDir'     , 'out'     , ...        % x- and y-tick labels are outside of the plot
82    'TickLength'  , [.02 .02] , ...
83    'YMinorTick'  , 'on'      , ...
84    'YGrid'       , 'on'      , ...        % only activate horizontal grid
85    'XColor'      , [.1 .1 .1], ...
86    'YColor'      , [.1 .1 .1], ...        % grid is dotted line and slightly grey
87    'YTick'       , -6000:1000:0, ...      % define grid, every 1000 m a grid line
88    'LineWidth'   , 1         );           % of linewidth = 1
89
90  % save the figure as usual
91  print('-depsc','-r300', '/home/hmaurice/Plots/
        global_mean_cumulative_vertical_heat_distribution_of_individual_ocean_basins');
```

```matlab
1  % --- Script for creating 3D plot for heat and thermal expansion --- %
2  % --- in dependence of temperature and salinity                 --- %
3
4  load('workspace_thermal_expansion_CCSM4_with_CT_rev5','ct', 'delta_temperature', ...
5      'so','heat_diff', 'RdYlBu');
6
7
8  ct = ct + delta_temperature - 273.15; % final conservative temperature values
9
10
11 A = reshape(ct,[1,7372800]); % make map array into 1*n array
12 B = reshape(so,[1,7372800]); % make map array into 1*n array
13 C = reshape(heat_diff,[1,7372800]); % make map array into 1*n array
14 D(:,1)= A; D(:,2) = B; D(:,3) = C; % create one big array
15
16
17 D(any(isnan(D),2),:)=[]; % remove any row that contains at leat one nan;
18 clear A B C;
19
20
21 A = D(:,1); B = D(:,2); C = D(:,3); % create the separate arrays again, this time
22                                     % they do not contain nan anymore
23
24
25
26
27 xi = linspace(min(A),max(A),40);    % create linear-spaced array for the x axis
28                                     % which include lowest and highest values of
29                                     % array A and 40 values inbetween
30 yi = linspace(min(B),max(B),40);
31 [XI YI] = meshgrid(xi,yi);          % create meshgrid out of the two axis arrays
32                                     % similar to mapping procedures earlier
33 ZI = griddata(A,B,C,XI,YI);         % ZI, the heat array is dependent on the ct, so
34                                     % values as well as the two axes
35                                     % defined
36
37
38
39 %% plotting
40
41 figure(1);
42 % RdYlBu = cbrewer('div', 'RdYlBu', 31);
43 % RdYlBu(16,:) = [1 1 1] % the colour in the middle is white
44 % Blues = cbrewer('seq', 'Blues', 15);
45 % RdYlBu(17:31,:) = Blues(1:15,:); % replace the blue shadings with better
46 %                                  % blue colours so those near 0 aren't
47 %                                  % yellow
48 colormap(flipud(RdYlBu));
```

```matlab
49  h = bar3(ZI); hold on;       % create bar graph
50
51  % smooth out the colours, for loop includes colouring the bars
52  shading interp;  % colour bars
53
54  set(h,'EdgeColor', [.3 .3 .3]) % bar border is grey
55  set(gca, 'Ydir', 'normal'); % flip salinity axis
56
57  % set axis labels
58  hXLabel = xlabel('Conservative Temperature [K]');
59  hYLabel = ylabel('Salinity [g / kg]');
60  hZLabel = zlabel('Heat Content [J]');
61
62  % set(gca, 'clim', [-8e17 8e17]);        % colour limit
63
64  h=colorbar; set(h, 'fontsize', 12, 'fontname', 'Times New Roman');
65  h1=ylabel(h,'Joule', 'color', [.3 .3 .3]);
66
67
68  set([hXLabel, hYLabel, hZLabel], ...
69      'FontName'    , 'Times New Roman');
70  set([hXLabel, hYLabel, hZLabel]  , ...
71      'FontSize'    , 12            );
72
73  % create grid and make the plot more fancy
74  set(gca, ...
75    'Box'          , 'off'      , ...
76    'TickDir'      , 'out'      , ...
77    'TickLength'   , [.02 .02] , ...
78    'XMinorTick'   , 'on'       , ...
79    'YMinorTick'   , 'on'       , ...
80    'ZMinorTick'   , 'on'       , ...
81    'YGrid'        , 'on'       , ...
82    'XColor'       , [.3 .3 .3], ...
83    'YColor'       , [.3 .3 .3], ...
84    'ZColor'       , [.3 .3 .3], ...
85    'LineWidth'    , 1          );
86
87  axis tight; % remove empty space
88  print('-depsc','-r400', '/home/hmaurice/Plots/volumetric_TS_plot');
```

Bibliography

Aagaard, K., Fahrbach, E., Meincke, J., and Swift, J. Saline outflow from the Arctic Ocean: Its contribution to the deep waters of the Greenland, Norwegian, and Iceland Seas. *Journal of Geophysical Research*, 96(20):433–441, 1991.

Antonov, J., Levitus, S., and Boyer, T. Thermosteric sea level rise, 1955–2003. *Geophysical Research Letters*, 32(12), 2005.

Armour, K. C., Marshall, J., Scott, J. R., Donohoe, A., and Newsom, E. R. Southern ocean warming delayed by circumpolar upwelling and equatorward transport. *Nature Geoscience*, 2016.

Bearman, G., Brown, J., and Team, O. C. *Ocean Circulation: Part of the Open University*, volume 3. Pergamon Press, 1989.

Bindoff, N. L., Willebrand, J., Artale, V., Cazenave, A., Gregory, J. M., Gulev, S., Hanawa, K., Le Quéré, C., Levitus, S., Yukihiro, N., Shum, C. K., Talley, L. D., and Unnikrishnan, A. S. Observations: Oceanic climate change and sea level. In *Climate Change 2007: The Physical Science Basis. Contribution of Working Group I to the Fourth Assessment Report of the Intergovernmental Panel on Climate Change*, volume 4, page 409. Cambridge University Press, Cambridge, United Kingdom and New York, NY, USA, 2007.

Boening, C., Willis, J. K., Landerer, F. W., Nerem, R. S., and Fasullo, J. The 2011 La Niña: So strong, the oceans fell. *Geophysical Research Letters*, 39(19), 2012.

Cannon, J. R. *The One-Dimensional Heat Equation*. Cambridge University Press, 1984.

Carton, J. A. and Santorelli, A. Global decadal upper-ocean heat content as viewed in nine analyses. *Journal of Climate*, 21(22):6015–6035, 2008.

Cazenave, A. and Llovel, W. Contemporary sea level rise. *Annual Review of Marine Science*, 2:145–173, 2010.

Church, J. A., Clark, P. U., Cazenave, A., Gregory, J. M., Jevrejeva, S., Levermann, A., Merrifield, M. A., Milne, G. A., Nerem, R. S., Nunn, P. D., Payne, A. J., Pfeffer,

W. T., Stammer, D., and Unnikrishnan, A. S. Sea level change. In *Climate Change 2013: The Physical Science Basis. Contribution of Working Group I to the Fifth Assessment Report of the Intergovernmental Panel on Climate Change [Stocker, T.F., D. Qin, G.-K. Plattner, M. Tignor, S.K. Allen, J. Boschung, A. Nauels, Y. Xia, V. Bex and P.M. Midgley (eds.)]*. Cambridge University Press, Cambridge, United Kingdom and New York, NY, USA., 2013.

Cooper, J. Release on the IAPWS Formulation 2008 for the Thermodynamic Properties of Seawater. *The International Association for the Properties of Water and Steam, September*, pages 1–19, 2008.

Douglas, B., Kearney, M. T., and Leatherman, S. P. *Sea level Rise: History And Consequences*, volume 75. Academic Press, 2000.

Drijfhout, S., Van Oldenborgh, G. J., and Cimatoribus, A. Is a decline of amoc causing the warming hole above the north atlantic in observed and modeled warming patterns? *Journal of Climate*, 25(24):8373–8379, 2012.

Durack, P. J., Gleckler, P. J., Landerer, F. W., and Taylor, K. E. Quantifying underestimates of long-term upper-ocean warming. *Nature Climate Change*, 4(11):999–1005, 2014.

Ekman, V. W. On the Influence of The Earth's Rotation on Ocean Currents. *Arkiv fÃŭr Matematik, Astronomi och Fysik*, 2:1–53, 1905.

England, M. H., McGregor, S., Spence, P., Meehl, G. A., Timmermann, A., Cai, W., Gupta, A. S., McPhaden, M. J., Purich, A., and Santoso, A. Recent intensification of wind-driven circulation in the Pacific and the ongoing warming hiatus. *Nature Climate Change*, 4(3):222–227, 2014.

Frölicher, T. L., Sarmiento, J. L., Paynter, D. J., Dunne, J. P., Krasting, J. P., and Winton, M. Dominance of the Southern Ocean in anthropogenic carbon and heat uptake in CMIP5 models. *Journal of Climate*, 28(2):862–886, 2015.

Gill, A. E. *Atmosphere-ocean dynamics*, volume 30. Academic press, 1982.

Gleckler, P. J., Durack, P. J., Stouffer, R. J., Johnson, G. C., and Forest, C. E. Industrial-era global ocean heat uptake doubles in recent decades. *Nature Climate Change*, 6(4): 394+, 2016.

Gregory, J. M. Vertical heat transports in the ocean and their effect on time-dependent climate change. *Climate Dynamics*, 16(7):501–515, 2000.

Gruber, N., Gloor, M., Mikaloff Fletcher, S. E., Doney, S. C., Dutkiewicz, S., Follows, M. J., Gerber, M., Jacobson, A. R., Joos, F., Lindsay, K., et al. Oceanic sources, sinks, and transport of atmospheric CO2. *Global Biogeochemical Cycles*, 23(1), 2009.

Gupta, A. S., Jourdain, N. C., Brown, J. N., and Monselesan, D. Climate drift in the cmip5 models. *Journal of Climate*, 26(21):8597–8615, 2013.

Heuzé, C., Heywood, K. J., Stevens, D. P., and Ridley, J. K. Southern Ocean bottom water characteristics in CMIP5 models. *Geophysical Research Letters*, 40(7):1409–1414, 2013.

Hofmann, M. and Rahmstorf, S. On the stability of the Atlantic meridional overturning circulation. *Proceedings of the National Academy of Sciences*, 106(49):20584–20589, 2009.

Jackett, D. R., McDougall, T. J., Feistel, R., Wright, D. G., and Griffies, S. M. Algorithms for density, potential temperature, conservative temperature, and the freezing temperature of seawater. *Journal of Atmospheric and Oceanic Technology*, 23(12):1709–1728, 2006.

Johnson, G. C. and Lyman, J. M. Oceanography: Where's the heat? *Nature Climate Change*, 4(11):956–957, 2014.

Kerr, R., Heywood, K., Mata, M., and Garcia, C. On the outflow of dense water from the Weddell and Ross Seas in OCCAM model. *Ocean Science*, 8(3):369, 2012.

Langehaug, H. R., Medhaug, I., Eldevik, T., and Otterå, O. H. Arctic/Atlantic Exchanges via the Subpolar Gyre. *Journal of Climate*, 25(7):2421–2439, 2012.

Lee, S.-K., Park, W., Baringer, M. O., Gordon, A. L., Huber, B., and Liu, Y. Pacific origin of the abrupt increase in Indian Ocean heat content during the warming hiatus. *Nature Geoscience*, 8(6):445–449, 2015.

Lenaerts, J., Le Bars, D., Kampenhout, L., Vizcaino, M., Enderlin, E. M., and Broeke, M. R. Representing Greenland ice sheet freshwater fluxes in climate models. *Geophysical Research Letters*, 42(15):6373–6381, 2015.

Levitus, S., Antonov, J. I., Boyer, T. P., Baranova, O. K., Garcia, H. E., Locarnini, R. A., Mishonov, A. V., Reagan, J., Seidov, D., Yarosh, E. S., et al. World ocean heat content and thermosteric sea level change (0–2000 m), 1955–2010. *Geophysical Research Letters*, 39(10), 2012.

Lyu, K., Zhang, X., Church, J. A., Slangen, A. B., and Hu, J. Time of emergence for regional sea-level change. *Nature Climate Change*, 4(11):1006–1010, 2014.

McDougall, T., Feistel, R., Millero, F., Jackett, D., Wright, D., King, B., Marion, G., Chen, C., Spitzer, P., and Seitz, S. The international thermodynamic equation of seawater 2010 (teos-10): Calculation and use of thermodynamic properties. *Global Ship-based Repeat Hydrography Manual, IOCCP Report*, 14, 2009.

McDougall, T. J. and Barker, P. M. Getting started with TEOS-10 and the Gibbs Seawater (GSW) oceanographic toolbox. *SCOR/IAPSO WG*, 127:1–28, 2011.

Moore, G., Pickart, R. S., Renfrew, I. A., and Våge, K. What causes the location of the air-sea turbulent heat flux maximum over the labrador sea? *Geophysical Research Letters*, 41(10):3628–3635, 2014.

Moore, G., Våge, K., Pickart, R., and Renfrew, I. Decreasing intensity of open-ocean convection in the Greenland and Iceland seas. *Nature Climate Change*, 5(6):1–6, 2015.

Morrison, A. K., Frölicher, T. L., and Sarmiento, J. L. Upwelling in the Southern Ocean. *Physics Today*, 68(1):27, 2015.

National Center for Atmospheric Research. CCSM4 CMIP 5 1850 - 2005 runs forcings information. http://www.cesm.ucar.edu/CMIP5/forcing_information/. [Accessed: 2016-06-23].

Pickart, R. S., Spall, M. A., Ribergaard, M. H., Moore, G., and Milliff, R. F. Deep convection in the Irminger Sea forced by the Greenland tip jet. *Nature*, 424(6945): 152–156, 2003.

Pithan, F. and Mauritsen, T. Arctic amplification dominated by temperature feedbacks in contemporary climate models. *Nature Geoscience*, 7(2):2–5, 2014.

Rahmstorf, S., Feulner, G., Mann, M. E., Robinson, A., Rutherford, S., and Schaffernicht, E. J. Exceptional twentieth-century slowdown in Atlantic Ocean overturning circulation. *Nature Climate Change*, pages 475–480, 2015.

Riva, R. E., Bamber, J. L., Lavallée, D. A., and Wouters, B. Sea-level fingerprint of continental water and ice mass change from GRACE. *Geophysical Research Letters*, 37 (19):1–6, 2010.

Roemmich, D., Johnson, G. C., Riser, S., Davis, R., Gilson, J., Owens, W. B., Garzoli, S. L., Schmid, C., and Ignaszewski, M. The Argo Program: Observing the global ocean with profiling floats. *Oceanography*, 22(2):34–43, 2009.

Schlesinger, M. E. et al. An oscillation in the global climate system of period 65-70 years. *Nature*, 367(6465):723–726, 1994.

Schmittner, A., Chiang, J. C., and Hemming, S. R. Introduction: The ocean's meridional overturning circulation. *Ocean Circulation: Mechanisms and Impacts-Past and Future Changes of Meridional Overturning*, pages 1–4, 2013.

Seager, R., Kushnir, Y., Naik, N. H., Cane, M. A., and Miller, J. Wind-Driven Shifts in the Latitude of the Kuroshio-Oyashio Extension and Generation of SST Anomalies on Decadal Timescales. *Journal of Climate*, 14(22):4249–4265, 2001.

Sinclair, K. E., Bertler, N. A., and Van Ommen, T. D. Twentieth-century surface temperature trends in the western Ross Sea, Antarctica: Evidence from a high-resolution ice core. *Journal of Climate*, 25(10):3629–3636, 2012.

Smith, R., Desflots, M., White, S., Mariano, A. J., and Ryan, E. H. *The Antarctic CP Current*, 2013. http://oceancurrents.rsmas.miami.edu/southern/antarctic-cp.html [Accessed: 19.06.2016].

Spall, M. A. and Pickart, R. S. Where Does Dense Water Sink? A Subpolar Gyre Example. *Journal of Physical Oceanography*, 31(3):810–826, 2001.

Talley, L. *North Atlantic circulation and water masses. Thermohaline forcing.*, 2000. http://sam.ucsd.edu/sio210/lect_5/lecture_5.html [Accessed: 09.06.2016].

Tipler, P. A. and Mosca, G. *Physics for scientists and engineers*. Springer-Verlag, 2007.

Umlauf, L. and Burchard, H. Diapycnal transport and mixing efficiency in stratified boundary layers near sloping topography. *Journal of Physical Oceanography*, 41(2): 329–345, 2011.

Van Vuuren, D. P., Edmonds, J., Kainuma, M., Riahi, K., Thomson, A., Hibbard, K., Hurtt, G. C., Kram, T., Krey, V., Lamarque, J.-F., et al. The representative concentration pathways: an overview. *Climatic Change*, 109:5–31, 2011.

Vertenstein, M., Craig, T., Middleton, A., Feddema, D., and Fischer, C. *CCSM4.0 User's Guide*, 2011. http://www.cesm.ucar.edu/models/ccsm4.0/ccsm_doc/ug.pdf [Accessed: 16.06.2016].

Winton, M., Takahashi, K., and Held, I. M. Importance of ocean heat uptake efficacy to transient climate change. *Journal of Climate*, 23(9):2333–2344, 2010.

Zhang, T. and Sun, D.-Z. ENSO asymmetry in CMIP5 models. *Journal of Climate*, 27 (11):4070–4093, 2014.